An experimental and numerical investigation of the combustion and heat transfer characteristics of hydrogen-fueled catalytic microreactors

Ran Sui [a], Nikolaos I. Prasianakis [a], John Mantzaras [a,*], Nithin Mallya [a], Jürgen Theile [a], Damien Lagrange [b], Martin Friess [c]

[a] Paul Scherrer Institute, Combustion Research, CH-5232 Villigen PSI, Switzerland
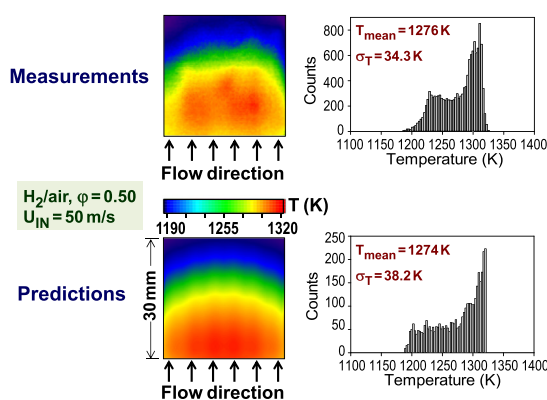[b] Microcertec, Pae de Lamirault-Collegien, 22 rue de Lamirault, 77090 Collegien, France
[c] German Aerospace Center (DLR), Institute of Structures and Design, Pfaffenwaldring 38-40, 70569 Stuttgart, Germany

HIGHLIGHTS

- Optimization of a six-channel H_2-fueled catalytic microreactor with 3D simulations.
- Counterflow configuration superior to coflow in spatial uniformity of temperatures.
- Simulations reproduce measured higher moments of surface temperature distributions.
- Maximum surface temperatures up to 1311 K and standard deviations up to 18.6 K.
- Radiation efficiencies up to 76%, suitable for microreactor coupling with TPVs.

GRAPHICAL ABSTRACT

ARTICLE INFO

ABSTRACT

The combustion and heat transfer characteristics of a hydrogen-fueled microreactor are investigated experimentally and numerically. The microreactor comprises a $30 \times 30 \times 4$ mm³ SiC-block equipped with six 1.5 mm diameter platinum channels. Combustion of fuel-lean H_2/air mixtures at equivalence ratios $\varphi = 0.25 - 0.50$ and inlet velocities 15–50 m/s is studied at coflow and counterflow configurations. Surface temperatures are measured with an infrared camera, while simulations are carried out with a 3D code that includes conjugate heat transfer, appropriate external heat losses, and detailed hetero-/homogeneous chemistry. Higher mass throughputs reduce the surface temperature spatial non-uniformities, while the onset of gaseous combustion lowers the catalyst surface temperatures and is thus detrimental for power generation applications. Four different channel configurations are tested for optimum temperature uniformity. Counterflow configurations are shown superior to the coflow configuration in attaining better surface temperature uniformities with standard deviations less than 19 K and maximum surface temperatures up to 1311 K. Comparisons of measurements and predictions are very favorable in terms of temperature probability density function (PDF) shapes and higher distribution moments. Counterflow configurations yield narrower PDFs slightly skewed to the low temperatures, while the coflow configuration yields mostly bimodal shapes. Radiation efficiencies increase with increasing inlet

---

* Corresponding author. Tel.: +41 56 3104046; fax: +41 44 3102199.
  E-mail address: ioannis.mantzaras@psi.ch (J. Mantzaras).

velocity and equivalence ratio. Application of the microreactor to power generation systems, in conjunction with thermoelectric devices, appears quite promising given the attained good spatial uniformity and the high values of surface temperatures.

1. Introduction

Hydrogen and hydrogen-containing fuels are under intense investigation for small- and large-scale power generation. Microreactors for small ($\sim$100 W_e) portable power generation devices fueled with hydrogen (Ghermay et al., 2010; Michelon et al., 2015; Norton et al., 2004; Seyed-Reihani and Jackson, 2004) or hydrogen-enriched hydrocarbons and syngas mixtures (Federici and Vlachos, 2011; Karagiannidis and Mantzaras, 2012; Seshadri and Kaisare, 2010) have been studied experimentally and numerically in the last years. In such systems hydrogen can be produced on-board from methane (Diehm and Deutschmann, 2014; Jiang et al., 2015; Kaisare et al., 2005; Stefanidis and Vlachos, 2009; Stefanidis et al., 2009) or high hydrocarbons (Casanovas et al., 2008; Donazzi et al., 2014; Eriksson et al., 2006; Hartmann et al., 2010; Holladay et al., 2004) using suitable microreformers. Most microreactors operate with heterogeneous (catalytic) combustion or with a variety of hybrid concepts, i.e. combined heterogeneous and homogeneous (gaseous) combustion (Schultze and Mantzaras, 2013), rather than with pure gaseous combustion. This is mainly dictated by the large surface-to-volume ratios of microreactors that result in much wider catalytic combustion stability envelopes compared to those of pure gaseous combustion (Ahn et al., 2005), the existence of a multitude of undesirable flame instabilities in tight geometrical confinements (Evans and Kyritsis, 2009; Fan et al., 2013; Kurdyumov et al., 2009; Pizza et al., 2010a) and the efficient suppression of such instabilities by coating the microreactor walls with a catalyst (Pizza et al., 2010b; Pizza et al., 2009).

Although hybrid reactor designs have distinct heterogeneous and homogeneous combustion zones with the former preceding the latter, gas-phase combustion cannot always be neglected inside the designated catalytic combustion zone. Even at the large geometrical confinements of practical catalytic microreactors (e.g. catalytic channels with sub-millimeter hydraulic diameters) gas-phase combustion can be appreciable for hydrocarbon fuels, depending on the pressure, temperature and residence time (Karagiannidis et al., 2011; Reinke et al., 2002). A detailed parametric study of fuel-lean H_2/air combustion in platinum-coated channels (tubular or planar) has delineated (Ghermay et al., 2011) the regimes of wall temperatures, inlet temperatures, pressures, and channel hydraulic diameters for which gaseous combustion amounts to at least 5% of the combined catalytic and gas-phase hydrogen conversion. Catalytic combustion of fuel-lean H_2/air mixtures is particularly challenging due to the diffusional imbalance of the deficient hydrogen reactant (Lewis number of hydrogen $Le_{H2} \sim 0.3$), which leads to superadiabatic surface temperatures (Bui et al., 1996; Mantzaras, 2014) that endanger the catalyst and reactor integrity. To mitigate such superadiabatic effects, an inverse hybrid concept for hydrogen has been recently proposed (Ghermay et al., 2010), whereby the gaseous combustion zone precedes the catalytic combustion zone.

Apart from microreactor applications, hybrid hetero-/homogeneous combustion of hydrogen is also of prime interest for large-scale power generation. One such approach is the catalytically stabilized thermal combustion (CST) (Carroni and Griffin, 2010), where part of the fuel is converted in a catalytic reactor and

the remaining is combusted in a subsequent gas-phase burner. The CST hybrid methodology mitigates flashback by hindering upstream flame propagation inside the catalytic module due to the inhibiting effect of heterogeneous reactions on homogeneous combustion (Mantzaras and Appel, 2002; Mantzaras and Benz, 1999). On the other side, post-combustion CO_2 capture techniques currently apply large flue gas recycle (FGR) in order to increase the CO_2 content in the exhaust and thus facilitate its subsequent capture (Schneider et al., 2007; Tan et al., 2006). For the post-combustion CO_2 capture methods, inclusion of an upstream catalytic reactor enhances the combustion stability of the less-reactive FGR-diluted fuel mixtures.

There is nowadays increased interest in developing renewable energy sources for satisfying rising electricity demands. An ideal power source should provide reliable and continuous base-load power as well as peak-load power when needed to match supply demand. This requires a high Annual Capacity Factor (ACF), which is the ratio of the source's realized output in one year to its potential output when operated at full capacity over the same period. Within the European Union project Hybrid Renewable energy Converter for continuous and flexible power production (HRC-Power, 2015) a combined solar/combustor microreactor is pursued, capable of operating either in sole combustion mode, sole solar mode, or mixed combustion/solar mode, with a targeted 95% ACF. Fig. 1 illustrates the concept, which comprises a central microreactor block (2) made from a high thermal conductivity material. Under solar operation alone, the top microreactor surface (1) is coated with a special absorbing layer to efficiently collect concentrated solar radiation, while the bottom surface is coated with a selectively emitting infrared radiation layer (e.g. to be coupled with a thermophotovoltaic (TPV) module). In the absence of solar radiation or in the case of intermittent solar radiation, combustion inside the microreactor supplies all or part of the thermal energy necessary to heat the selectively IR-emitting bottom surface. A number of such microreactors can eventually be
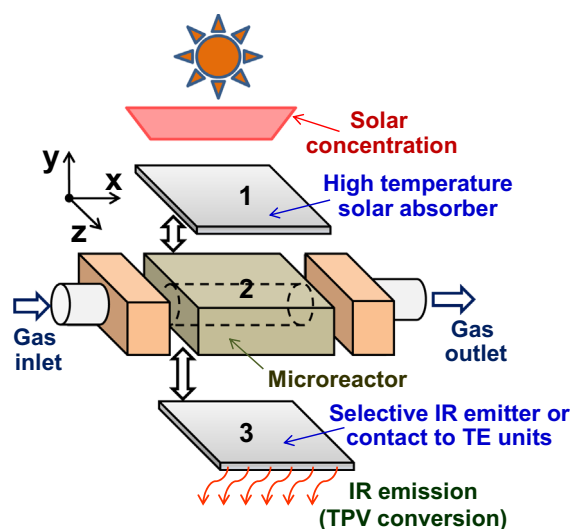

Fig. 1. Schematic of the solar/combustion reactor: (1) solar-energy-absorbing top surface, (2) microreactor block, and (3) IR-emitting bottom surface.
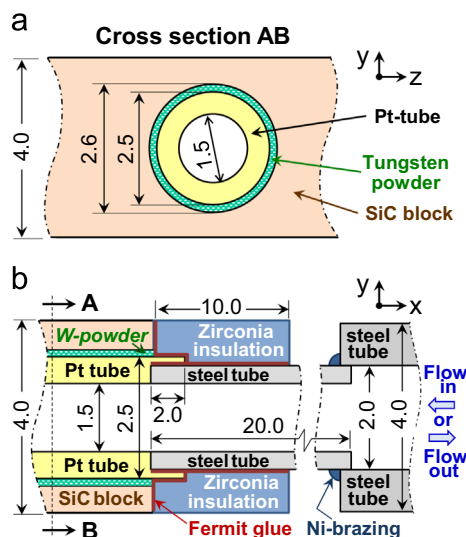
Fig. 2. (a) Cross section of the microreactor showing one catalytic channel, (b) details of the catalytic channel inlet/outlet arrangement. All dimensions are in mm.
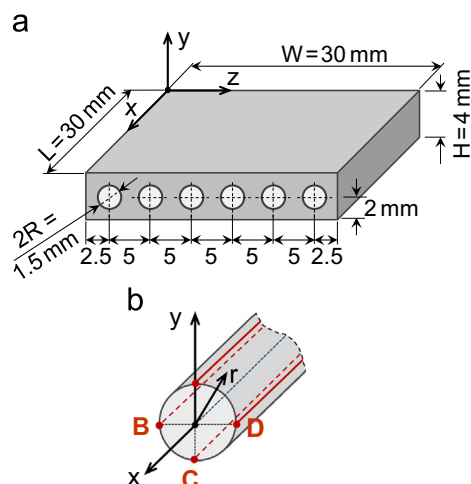

Fig. 3. (a) Microreactor geometry with six-channel arrangement, (b) individual channel details relevant for the numerical model.

clustered to create a larger power unit ($\sim$10 kW radiation emitting power). Requirements for this concept are surface temperatures in excess of 1000 °C with corresponding spatial uniformities around $\pm$50 °C.

Catalytic rather than gaseous combustion is the opted method, with appropriate catalytic channels manufactured inside the microreactor block. Catalytic combustion facilitates efficient heat transfer from the reacting channel surfaces to the outside faces of the microreactor block. Catalytic and non-catalytic microreactors have been studied in the past in combination with thermoelectric, piezoelectric and thermophotovoltaic generators for electricity production (Ahn et al., 2005; Kamijo et al., 2009; Kyritsis et al., 2004; Li et al., 2013; Um et al., 2014; Yang et al., 2012; Yoshida et al., 2006). Optimization of temperature uniformity has not been the main focus of previous catalytic microreactors: reported temperature differences across the catalytic burner were 150 K in Kyritsis et al. (2004) and 200 K in Kamijo et al. (2009) for operation at moderate reactor temperatures of 1100 K.

The present work undertakes an experimental and numerical investigation of the combustion processes in a microreactor equipped with six platinum tubes and operated with fuel-lean H$_2$/

air mixtures (equivalence ratios $\varphi=0.25$–0.50). Sole combustion operation is herein studied, without coupling to solar radiation and to special absorbing/emitting surface layers. Using fundamental knowledge from the catalytic combustion characteristics of hydrogen (superadiabatic surface temperatures, dependence of superadiabaticity on channel length) optimization of the channel flow configuration is carried out using 3D simulations with detailed chemistry and conjugate heat transfer in the solid. Goals are to demonstrate a reactor design with maximum surface temperatures in excess of 1000 °C and temperature variations around $\pm$50 °C. Specific objectives are to investigate the impact of inlet mass flow rate and equivalence ratio on the attained surface temperatures, to expose the underlying catalytic combustion process and to assess the radiation efficiency of the microreactor.

This article is organized as follows. In Section 2 the experimental configuration is described while in Section 3 the 3D numerical model is elaborated. In Sections 4.1 and 4.2 fundamental properties of hydrogen catalytic combustion, which are relevant for the microreactor design, are reviewed. Optimization of the microreactor catalytic channel configuration is discussed in Section 4.3, comparisons between measurements and predictions follow in Section 4.4 and the ensuing radiation efficiency is presented in Section 4.5. Conclusions are finally summarized in Section 5.

2. Experimental

2.1. Catalytic reactor assembly

The reactor comprises a $30 \times 30 \times 4$ mm^3 SiC block with six straight cylindrical channels (2.6 mm in diameter and 30 mm in length) and six platinum tubes (99.95% Pt purity, supplied by Wieland Edelmetalle, Germany) each with an outer diameter (OD) of 2.5 mm and an inner diameter (ID) of 1.5 mm. The Pt tubes are inserted inside the SiC channels and the resulting 50 μm radial gaps are filled with tungsten powder (average particle size 3 μm), as illustrated in Fig. 2a.

The tungsten powder accommodates the different thermal expansion of the SiC and Pt materials and at the same time allows for efficient heat transfer between the Pt tube and the SiC block. The geometry of the solid and void parts of the integrated reactor is depicted in Fig. 3a. It is further noted that the use of solid platinum tubes and not of a technical catalyst (i.e. supported Pt-catalyst deposited on the SiC channels) is dictated by the need to maintain, for this demonstration study, constant catalytic properties: in technical catalysts there is always an inherent drop of reactivity during long-term operation due to loss of active catalyst.

The Pt tubes are 34 mm long, protruding 2 mm from each side of the SiC block (see Fig. 1b). Over the 2 mm extended lengths, the Pt tubes have an enlarged ID of 2 mm in order to facilitate connection to six external steel tubes (high temperature stainless steel 1.4401) with 1.5 mm ID, 2 mm OD and 20 mm length. The steel tubes either supply reactants to the reactor or direct the combustion products to the exhaust. The gas entry and exit faces of the reactor are insulated by two 10-mm-long zirconia blocks, while all connections are sealed with temperature-resistant (up to 1100 °C) Fermit glue (see Fig. 1b). The resulting arrangement is tight as firstly determined by leak-proof tests at room temperature and then by positioning a high-sensitivity hydrogen detector in the proximity of the inlet and exhaust during actual reactor operation. A photograph of various components before sealing the reactor assembly is shown in Fig. 4.

The SiC block (see Fig. 4) is manufactured by pressing and sintering of a bulk ceramic. Grinding and polishing operations are then necessary to reach the required dimensions that cannot be
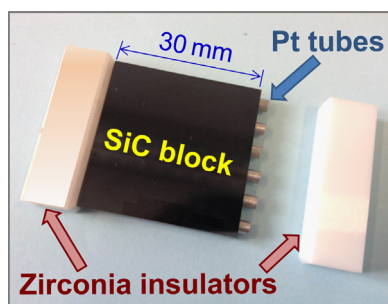
Fig. 4. Photograph of microreactor parts.

directly achieved by sintering. Due to the hardness of sintered SiC, firstly only an approximate shape with six holes is constructed. A $32 \times 32 \times 6$ mm^3 SiC block is pressed, drilled to create the 2.5 mm diameter holes, and then sintered at high temperature. Subsequently, two major grinding operations are performed to finalize the geometry. The six holes are bored to increase their final diameters to 2.6 mm and to insure the straightness of each hole. This requires several diamond core-drilling tools with diameters from 2.5 to 2.6 mm. The thickness of the block is then ground down from 6 to 4 mm. At the end of the process, only 1–2 μm are removed at each grinding pass in order to get an initially smooth surface finish. The roughness R_a reaches at this stage about 0.4–0.6 μm and the surface has no defects (spots, cracks).

A double-face polishing is finally made on a flat polishing machine. The pressed SiC is particularly convenient for polishing as it is very hard (with HV(1 kg) of 25 GPa) and made of small particles 1-10 μm in size. During polishing, the parts turn onto a grinding disc and are immersed into a fluid with diamond particles of 1 to 2 μm size in suspension. The pressure applied on the parts from above is slowly ramped along the process. This enables a uniform surface finish without any stress or scratch, which is further crucial for achieving uniform radiation emission characteristics. The attained roughness R_a is better than 0.05 μm on the 30×30 mm^2 surfaces.

2.2. Test rig

The test rig is shown in Fig. 5. The total flow rates of hydrogen and air are controlled by two dedicated Brooks mass flow controllers (MFC), using SIEMENS hardware/software. High purity hydrogen (99.995%) and air are supplied by pressurized bottles and an oil-free compressor, respectively. The hydrogen and air flows are split and controlled by 2×6 ball-valve flowmeters. Each of the twelve flowmeters can be independently adjusted to ensure equal flowrates in every channel. Mixing of hydrogen and air is achieved first by meshes and then by six 1.5-meter-long plastic supply tubes with 3.5 mm ID. The plastic tubes are connected to six 4 mm OD and 2 mm ID steel tubes of 100 mm length, which are in turn nickel-brazed to the 2 mm OD inner stainless steel tubes (see Fig. 1b). The reactor assembly is fixed by two metal clamps, which hold snug-tight the inlet and outlet metal tubes with an intervening insulating ceramic fiber.

To facilitate catalytic ignition, external preheating of the reactant supply steel tubes and the SiC reactor is provided by one (or two, depending on the specific flow direction in the six channels) electric heating air guns. Following ignition, the air heating guns are removed and vigorous combustion is self-sustained. The top 30×30 mm^2 surface temperature distribution of the SiC block is measured by a FLIR infrared camera (Type A655sc, 640×480 pixel chip, range of temperature -40 to 1200 °C) as shown in Fig. 5. The camera chip records the 30×30 mm^2 top SiC surface onto 125×125 pixels. An input parameter required by the FLIR camera is
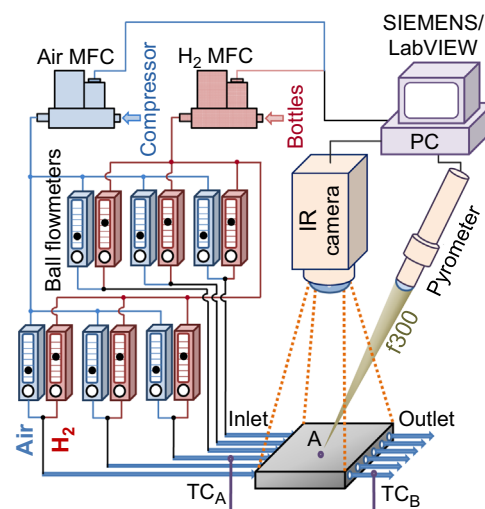

Fig. 5. Schematic of the test rig with the microreactor, the infrared (IR) camera, the mass flow controllers (MFC), the ball flowmeters, the pyrometer and thermocouples (TC).

the surface emissivity, which is independently assessed by a two-color pyrometer (Maurer AG, type QKTRD1475, temperature range 400 to 1300 °C). The two-color pyrometer collects the radiation emitted from a 0.2 mm^2 circular spot at the center of the 30×30 mm^2 top SiC surface, by means of an f-300 mm objective lens and a laser-light focusing indicator. Pyrometer measurements consider a gray-body behavior for the emitting surface and take the ratio of the emitted intensities at two different wavelength bands (1.40–1.75 μm and 1.60–1.75 μm), thus canceling the impact of the specific surface emissivity. The gray-body emitting behavior of the SiC block is verified independently, by comparing the two-color pyrometer measurements to thermocouple measurements when the block is inserted in a high-temperature (400–1000 °C) oven.

The inlet and outlet gas temperatures are measured by K-type thermocouples. These temperatures are used as boundary conditions in the numerical simulations and also allow for safety control by monitoring the exhaust gas temperature. National Instruments hardware in conjunction with LabVIEW software records the flow rates, fuel/air equivalence ratio, surface emissivity and temperatures.

3. Numerical

Steady numerical simulations are carried out using the OpenFOAM code (OpenFOAM, 2014) for modeling the 3D solid heat conduction and the heat losses from the outer SiC surfaces, in conjunction with a parabolic (boundary layer) 2D reactive CFD code for simulating the catalytic channels. A similar approach has been recently reported for modeling the catalytic partial oxidation of methane in a honeycomb structure (Hettel et al., 2015).

3.1. Catalytic channel model

A 2D steady parabolic code is used to model combustion in the 1.5 mm diameter catalytic channels. The latest version of the employed parabolic channel solver is detailed in Zheng and Mantzaras (2014). For the present high flow rates (inlet Reynolds numbers 830–2750 based on the channel diameter $2R = 1.5$ mm) the boundary layer approximation is justified. Specifically, it has been demonstrated that the boundary layer approximation is valid for channel-flow catalytic combustion at Reynolds numbers as low as 50 (Raja et al., 2000). For combined catalytic and gas-phase combustion, we have shown (Mantzaras et al., 2000) that the

requirements for validity of the boundary layer approximation are more stringent. However, in the present study the contribution of gas-phase chemistry is negligible, as will be discussed in the forthcoming Section 4.2. Finally, given the present high channel surface temperatures, a laminar flow model suffices: it has been shown (Appel et al., 2005; Appel et al., 2002b) that the strong flow laminarization induced by the hot catalytic walls guarantees laminar flow conditions even for inlet Reynolds numbers in excess of 4000 as long as the wall temperatures are above 1000 K.

The steady-state continuity, momentum, species, and energy conservation equations in cylindrical coordinates become, under the boundary layer approximation, as follows:

$$\frac{\partial \rho u}{\partial x} + \frac{1}{r}\frac{\partial r \rho v}{\partial r} = 0, \tag{1}$$

$$\rho u \frac{\partial u}{\partial x} + \rho v \frac{\partial u}{\partial r} = -\frac{\partial p}{\partial x} + \frac{1}{r}\frac{\partial}{\partial r}\left(\mu r \frac{\partial u}{\partial r}\right), \tag{2}$$

$$\frac{\partial p}{\partial r} = 0, \tag{3}$$

$$\rho u \frac{\partial Y_k}{\partial x} + \rho v \frac{\partial Y_k}{\partial r} = \frac{1}{r}\frac{\partial r \rho V_{k,r} Y_k}{\partial r} + \dot{\omega}_k W_k, \quad k = 1, .2, ..K_g, \tag{4}$$

$$\rho c_p \left(u\frac{\partial T}{\partial x} + v\frac{\partial T}{\partial r}\right) - \frac{1}{r}\frac{\partial}{\partial r}\left(\lambda_g r \frac{\partial T}{\partial r}\right) + \sum_{k=1}^{K_g} c_{p,k}\rho V_{k,r} Y_k \frac{\partial T}{\partial r} = -\sum_{k=1}^{K_g} h_k \dot{\omega}_k W_k. \tag{5}$$

The set of Eqs. (1)–(5) is supplemented by the ideal gas law:

$$p = \rho \frac{R^0}{\overline{W}}T. \tag{6}$$

At each channel inlet ($x=0$) the temperature, species mass fractions and velocity are given. Symmetry boundary conditions are applied at the channel centerline ($r=0$). At the gas-wall interface ($r=R$) no-slip is applied ($u=v=0$), while the energy boundary condition is:

$$T = T_w(x), \tag{7}$$

whereby the axial wall temperature profile $T_w(x)$ of every channel is supplied by the OpenFOAM computation, as will be discussed in Section 3. The gas-phase species interfacial boundary conditions are:

$$(\rho Y_k V_{k,r})_{r=R} = \dot{s}_k W_k. \tag{8}$$

The surface species coverages are calculated from the following algebraic equations:

$$\sigma_m \frac{\dot{s}_m}{\Gamma} = 0, \quad m = 1, 2, ...K_s, \tag{9}$$

where the surface reaction rates $\dot{s}_m$ are given by:

$$\dot{s}_m = \sum_{\ell=1}^{N_s} \nu_{m\ell} k_{f_\ell} \prod_{j=1}^{K_g+K_s} C_j^{\nu'_{j\ell}}, \tag{10}$$

with N_s the number of surface reactions and $\nu_{m\ell}$ the stoichiometric coefficient of species m in surface reaction ℓ. For gaseous species ($j=1, 2,.. K_g$) the concentrations in Eq. (10) are $C_j = \rho Y_j/W_j$ (mol/cm^3), whereas for surface species ($j=1, 2,.. K_s$) the corresponding concentrations are $C_j = \Gamma \theta_j/\sigma_j$ (mol/cm^2). The reaction rate coefficients k_{f_ℓ} in Eq. (10) are:

$$k_{f_\ell} = A_\ell T^{\beta_\ell} \exp\left(\frac{-E_\ell}{RT}\right)\prod_{i=1}^{K_s}\theta_i^{\mu_{i\ell}}\exp\left(\frac{\varepsilon_{i\ell}\theta_i}{RT}\right), \tag{11}$$

where A_ℓ, β_ℓ and E_ℓ denote the pre-exponential, temperature exponent, and activation energy of surface reaction ℓ, respectively. The parameters $\varepsilon_{i\ell}$ and $\mu_{i\ell}$ introduce coverage dependencies on the reaction rate coefficient, which account for variations in the

adsorption binding states due to changing surface coverage (Coltrin et al., 1996).

The employed numerical diffusion velocity vectors $\overrightarrow{V}_k$ in Eqs. (4) and (5) are:

$$\overrightarrow{V}_k = \overrightarrow{V}_k^* + \overrightarrow{V}_c. \tag{12}$$

A mixture-average diffusion model, including thermal diffusion for the light species H and H$_2$, is adopted (Kee et al., 1996a) for the diffusion velocity vectors $\overrightarrow{V}_k^*$:

$$\overrightarrow{V}_k^* = -D_{km}\overrightarrow{\nabla}\left[\ln(Y_k\overline{W}/W_k)\right] - \left[D_k^T/(\rho Y_k)\right]\overrightarrow{\nabla}(\ln T). \tag{13}$$

In Eq. (12), $\overrightarrow{V}_c$ is a correction velocity (Coltrin et al., 1996) introduced to numerically guarantee mass conservation:

$$\overrightarrow{V}_c = -\sum_{k=1}^{K_g} Y_k \overrightarrow{V}_k^*. \tag{14}$$

The set of Eqs. (1)–(6) and (9) subject to the boundary conditions of Eqs. (7) and (8) constitutes a parabolic system of differential-algebraic equations (DAE), which is solved numerically using the DASSL package (Brenan et al., 1989). Finite difference approximations on a non-uniform radial grid are applied to discretize the governing equations. DASSL performs integration in the streamwise x-direction using an implicit stepping method with adaptive spacing. Marching in x-direction yields the solution down to the desired streamwise distance.

The detailed catalytic reaction mechanism of hydrogen oxidation over platinum from Deutschmann et al. (2000) is employed (11 irreversible and 3 reversible reactions, 5 surface and 9 gaseous specious). For homogenous chemistry, the H$_2$/O$_2$ mechanism from Burke et al. (2012) (21 reversible reactions and 9 species) is used with its accompanying gas phase thermodynamic data. The aforementioned catalytic and gas-phase reaction mechanisms have reproduced measured catalytic conversions and homogeneous ignition distances in fuel-lean and fuel-rich H$_2$/air combustion over Pt (Ghermay et al., 2010; Ghermay et al., 2011; Mantzaras et al., 2009; Schultze et al., 2013).

Surface and gas-phase reaction rates are evaluated using Surface-CHEMKIN (Coltrin et al., 1996) and CHEMKIN respectively (Kee et al., 1996b), while transport properties are calculated from the CHEMKIN database (Kee et al., 1996a).

3.2. Solid heat transfer model

The 3D heat conduction inside the SiC solid and the external heat losses are computed with open source software OpenFOAM (OpenFOAM, 2014). Steady state heat conduction in the solid follows the equation:

$$\frac{\partial}{\partial x}\left(\lambda_s\frac{\partial T}{\partial x}\right) + \frac{\partial}{\partial y}\left(\lambda_s\frac{\partial T}{\partial y}\right) + \frac{\partial}{\partial z}\left(\lambda_s\frac{\partial T}{\partial z}\right) = 0. \tag{15}$$

The solid thermal conductivity λ_s accounts for the composite solid domain (SiC, tungsten, and platinum, see Fig. 2a). Simple 1D heat transfer simulations have shown that the 50 μm thick tungsten powder layer can be modeled, without loss of accuracy, either as Pt or SiC material (Table 1 provides the thermal conductivities of the three materials as well as an estimated value (Woodside and Messmer, 1961) for the thermal conductivity of the 50-μm-thick porous medium considering it as consisting of spherical tungsten particles). Characteristically, for 1D heat transfer in a 1.25 mm thick slab comprising 0.5 mm Pt, 0.05 mm tungsten and 0.7 mm SiC (i.e. mimicking the geometry in Fig. 2a) where the bottom slab side (Pt) is fixed at 1250 K and the top side (SiC) has a heat loss h ($T-T_\infty$) with $h=500$ W m^{-2} K^{-1} and $T_\infty=300$ K, the computed top side temperature of the slab varies by less than 0.4 K when using

Table 1
Thermal conductivity of solid materials.

Material	Thermal conductivity (W m⁻¹ K⁻¹)
Silicon carbide[a]	$\Sigma_{k=0}^{k=5} \alpha_k T^k$
Platinum[b]	$\beta_0 + \beta_1 T$
Tungsten solid	110
Tungsten porous layer	40

[a] The SiC thermal conductivity varies from 266 $W\,m^{-1}\,K^{-1}$ at 300 K to 56 $W\,m^{-1}\,K^{-1}$ at 1350 K. Over the range 800–1350 K, which is of interest in the present study, the variation is from 97.9 to 56.8 $Wm^{-1}K^{-1}$ and is modeled by a fifth-order polynomial function of temperature: $a_0 = $ 806.10 $Wm^{-1}K^{-1}$, $a_1 = $ -3.155 $W\,m^{-1}\,K^{-2}$, $a_2 = $ 6.109 × 10⁻³ $W\,m^{-1}\,K^{-3}$, $a_3 = $ -6.204 × 10⁻⁶ $W\,m^{-1}\,K^{-4}$, $a_4 = $ 3.140 × 10⁻⁹ $W\,m^{-1}\,K^{-5}$, $a_5 = $ −6.220 × 10⁻¹³ $W\,m^{-1}\,K^{-6}$.

[b] In the range 800–1350 K the thermal conductivity of platinum varies from 74.7 to 84.8 $W\,m^{-1}\,K^{-1}$ and is modeled by a linear function of temperature: $\beta_0 = $ 60.19 $W\,m^{-1}\,K^{-1}$, $\beta_1 = $ 0.0182 $W\,m^{-1}\,K^{-2}$.

for the 50 μm layer any of four thermal conductivities given in Table 1. The high $h = 500$ W m⁻² K⁻¹ is selected to exemplify the temperature difference across the slab. In the ensuing simulations the tungsten powder is modeled as SiC, thus eliminating the excessive grid required to resolve the 50 μm thick tungsten layer.

The solid geometry is discretized to 5.8 million tetrahedral cells, which are further refined at near-channel regions. This results to 28,000 cell surfaces on every channel (see Fig. 6), ensuring grid-independent and smooth temperature distributions. At the channel surfaces, which are interfaces between the fluid and solid, the heat fluxes are calculated by the CFD catalytic combustion code and then passed to OpenFOAM as explained below. The interfacial solid/gas energy balance in the channel is:

$$\sum_{k=1}^{Kg} (h_k \dot{s}_k W_k)_{r=R} - \lambda_g \frac{\partial T}{\partial r}\bigg|_{r=R_-} + \lambda_s \frac{\partial T}{\partial r}\bigg|_{r=R_+} = 0. \qquad (16)$$

The CFD code provides the first two terms in the left side of Eq. (16) (heat generation via surface reactions and convection). This allows evaluation of the third term in the left side of Eq. (16) (heat conduction in the solid), which is then passed to the OpenFOAM as Neumann boundary condition.

At the entry and outlet sides of the reactor ($x = 0$ and $x = L$ in Fig. 3a) the boundary conditions include conductive heat losses through the zirconia insulators and the 2 mm OD stainless steel connecting tubes (see Fig. 2b), with thermal conductivities 2 $Wm^{-1}K^{-1}$ and 26 $Wm^{-1}K^{-1}$, respectively. To this direction, temperatures at the exposed vertical faces of the zirconia blocks and at the steel tube external surfaces (located axially 10 mm after the end of the SiC block, see Fig. 2b) are measured during experiments with K-type thermocouples. These temperatures are then used to estimate the conductive heat losses by assuming a linear temperature drop over the 10 mm length from the SiC/zirconia interfaces down to the end of the zirconia blocks. At the other fully exposed four surfaces i.e. top, bottom, left and right surfaces, both convective and radiative heat losses are accounted for:

$$\lambda_s \frac{\partial T}{\partial n}\bigg|_{\partial\Omega_-} + h(T - T_\infty) + \varepsilon\sigma\left(T^4 - T_\infty^4\right) = 0, \qquad (17)$$

with n the local normal to the infinitesimal surface element $\partial\Omega$, T the local surface temperature and $T_\infty = 300$ K. The heat loss coefficients h at the outer surfaces are taken from ASHRAE (2009) and refer to a quiescent environment: $h = 21.6$ $Wm^{-2}K^{-1}$ for the top 30 × 30 mm² surface, $h = 10$ $Wm^{-2}K^{-1}$ for the bottom 30 × 30 mm² surface and $h = 30.7$ $Wm^{-2}K^{-1}$ for the 4 × 30 mm² vertical sides. For the radiative heat loss, the surface emissivity is supplied from the experiments and it typically varies from 0.60 to 0.65. Due to its fourth order dependence on surface temperature, the radiative heat loss aggravates numerical convergence. This is remedied by using
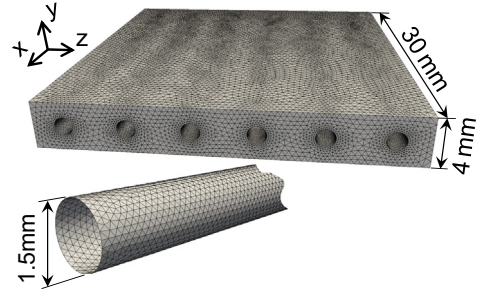
Fig. 6. 3D discretization of the microreactor solid domain.

under-relaxation and forcing many sub-iterations for every main iteration step of the reactive flow-solid coupling procedure.

3.3. Coupling of solid and flow solvers

The reactive flow code and the solid heat transfer/external heat loss code are coupled iteratively until a converged steady state solution is achieved. The combustion code uses the channel wall temperatures as input and calculates the heat fluxes at the channel surface, while the OpenFOAM calculation uses wall heat fluxes as input and calculates the temperature distributions in the solid and the external surfaces. Interfaces between the combustion code and OpenFOAM have been implemented as two Python codes. To avoid overshooting of numerical iterations, under-relaxation is necessary. After every combustion computation, the heat fluxes are under-relaxed with a user-defined factor before they are passed to OpenFOAM computation.

In the 3D simulation due to the non-axisymmetric channel surface temperature distribution, a simple 2D channel combustion calculation is not truly exact. The maximum peripheral channel surface temperature variation is, at any axial location, typically less than 15 K and this allows for the construction of the following quasi-3D model. To extend the 2D computations to 3D, four combustion calculations are performed for every channel (corresponding to the axial lines A, B, C and D in Fig. 3b). In the four 2D combustion calculations, the wall temperature boundary condition is imported from OpenFOAM at the top (A), left (B), bottom (C) and right (D) locations of the channel surface, respectively. Afterwards, the generated four wall heat flux distributions are interpolated to create one 3D cylindrical distribution which is subsequently passed to the OpenFOAM 3D as Neumann boundary input. The same approach has been recently adopted in Hettel et al. (2015), however, for catalytic channels having square cross sections.

To achieve faster computation, parallel computing is applied. Six channels are calculated in parallel at each iteration step. Similarly, the solid reactor is also decomposed into six parts for parallel computing with OpenFOAM. Convergence is typically achieved in 30-40 iterations.

4. Results and discussion

Fundamental properties of the hetero-/homogeneous combustion of fuel-lean H_2/air mixtures over platinum are firstly discussed, in order to facilitate the ensuing discussion on the selected operating conditions of the microreactor and the optimization strategy for the channel configuration. Comparisons between measured and predicted surface temperature distributions for the selected configurations are subsequently presented and finally radiation efficiencies are computed.

4.1. Surface temperatures in hydrogen hetero-/homogeneous combustion

The diffusional imbalance of hydrogen (the Lewis number of the deficient hydrogen reactant is less than unity in fuel-lean H_2/air mixtures) leads to catalyst surface temperatures significantly higher than the adiabatic equilibrium temperature of the reactive mixture. Considering first a catalytic flat plate rather than a channel, it can be formally shown (Zheng and Mantzaras, 2014) that under the conditions of adiabaticity, infinitely-fast catalytic chemistry and in the absence of gaseous chemistry, the wall temperature T_w is constant along the catalytic flat plate and equal to:

$$T_w = T_\infty + Le_{H2}^{-2/3}(\Delta T)_c, \qquad (18)$$

where Le_{H2} is the Lewis number of the deficient hydrogen, T_∞ is the free-stream temperature, and $(\Delta T)_c$ is the adiabatic combustion temperature rise:

$$(\Delta T)_c = T_{ad} - T_\infty \equiv Y_{H_2,\infty}Q_{H_2}/c_p, \qquad (19)$$

with T_{ad} the adiabatic equilibrium temperature of the free-stream H_2/air mixture, $Y_{H2,\infty}$ the free-stream mass fraction of hydrogen and Q_{H2} the heat of combustion per unit mass of hydrogen. Eqs. (18) and (19) indicate that $T_w = T_{ad}$ is satisfied only when $Le = 1$. For fuel-lean H_2/air mixtures whereby $Le_{H2} \approx 0.3$ the wall temperature always attains superadiabatic values, $T_w > T_{ad}$.

Contrary to the catalytic flat plate, the wall temperature in the confined channel-flow geometry (again under the conditions of adiabaticity, infinitely-fast catalytic chemistry and absence of gaseous chemistry) is not constant along the streamwise direction: the superadiabatic flat-plate solution in Eq. (18) is recovered only at the channel entry ($x \to 0$), whereas farther downstream the wall temperature drops with increasing x-distance and reaches the adiabatic equilibrium temperature T_{ad} only upon complete hydrogen consumption. To clarify this behavior, streamwise profiles of computed wall temperatures and mean gas temperatures are presented next for a tubular channel with similar geometrical characteristics as the Pt tubes in Fig. 2a (1.5 mm ID, length 30 mm, but with a smaller OD of 1.6 mm leading to a wall thickness $\delta = 0.05$ mm, see the inset figure in Fig. 7). Inlet conditions refer to an H_2/air mixture with $\varphi = 0.40$, $T_{IN} = 300$ K, $U_{IN} = 15$ m/s and $p = 1$ bar. The outer channel walls are considered adiabatic.

A 2D Navier-Stokes reactive CFD code is used to simulate the flow and the solid heat conduction; model details have been provided elsewhere (Ghermay et al., 2010; Karagiannidis et al., 2011). A mesh of 150×48 points for the gas (30×0.75 mm^2) and 150×20 points for the solid (30×0.05 mm^2) is sufficient to provide a grid-independent solution.

Computations are shown in Fig. 7, for three different cases marked 1–3. Case 1 is adiabatic (no heat loss from the 1.6 mm OD tube outer surfaces or from the entry/outlet vertical solid faces), while heat conduction in the solid wall is not accounted for in order to avoid redistribution of energy along the channel. The interfacial energy boundary condition of Eq. (16) reduces to a convection/reaction balance:

$$\sum_{k=1}^{Kg} (h_k \dot{s}_k W_k)_{r=R} - \lambda_g \frac{\partial T}{\partial r}\Big|_{r=R_-} = 0. \qquad (20)$$

Physically, Case 1 simulates a tubular channel with a solid wall having $\lambda_s = 0$. Case 1 is computed with catalytic chemistry (C) only (no gas-phase chemistry), which is additionally considered infinitely-fast. Numerically this is achieved by using a single-step catalytic reaction $H_2 + \frac{1}{2}O_2 \to H_2O$ with the following interfacial species boundary conditions (see Zheng and Mantzaras (2014)):

$$Y_{H_2}(r=R) = 0, \text{ and} \qquad (21)$$
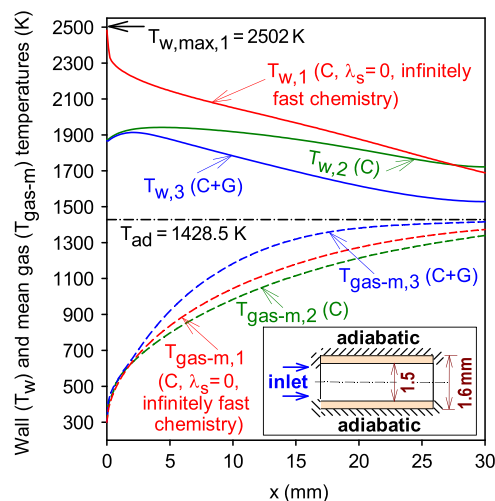
Fig. 7. Computed wall temperatures (T_w) and mean gas temperatures (T_{gas-m}) in a Pt-coated cylindrical channel with 30 mm length, 1.5 mm internal diameter, 1.6 mm outside diameter and adiabatic outer walls (geometry shown in the inset figure). Three simulations are shown: (1) infinitely fast catalytic (C) chemistry (no gaseous chemistry) and no heat conduction in the solid, (2) detailed catalytic (C) reaction mechanism (no gaseous chemistry) with heat conduction in the solid, (3) detailed catalytic and gas-phase (C+G) reaction mechanisms with heat conduction in the solid. H_2/air combustion with $\varphi = 0.40$, $T_{IN} = 300$ K, $U_{IN} = 15$ m/s, $p = 1$ bar. The horizontal line marked T_{ad} defines the adiabatic equilibrium temperature of the incoming mixture.

$$(\rho Y_k V_{k,r})_{r=R} = \frac{(\nu_k' - \nu_k'')W_k}{W_{H_2}}(\rho Y_{H_2}V_{H_2,r})_{r=R}, k = O_2, H_2O, N_2, \qquad (22)$$

with ν_k', ν_k'' the stoichiometric coefficients of the k-th species in the reactants and products, respectively. The boundary conditions in Eqs. (21) and (22) are equivalent to those in Eq. (8) in the limit $\dot{s}_k \to \infty$, and ensure infinitely-fast catalytic conversion of the deficient hydrogen reactant. The computed maximum wall temperature in Case 1 is $T_{w,max,1} = 2502$ K and occurs at the channel entry ($x = 0$). This temperature is 1073.5 K above the adiabatic equilibrium temperature $T_{ad} = 1428.5$ K (referring to a $\varphi = 0.40$ H_2/air mixture at $T_{IN} = 300$ K). Moreover, the computed $T_{W,max,1} = 2502$ K is in good agreement with the theoretical flat plate solution $T_w = 2513$ K calculated from Eq. (18), using $Le_{H2} = 0.364$ (evaluated using the Chemkin transport package (Kee et al., 1996a)). The wall temperature $T_{w,1}$ drops monotonically with increasing streamwise distance, while the mean gas temperature $T_{gas-m,1}$ increases with increasing streamwise distance; both $T_{w,1}$ and $T_{gas-m,1}$ approach the adiabatic equilibrium temperature T_{ad} upon complete conversion of hydrogen. For Case 1, the hydrogen conversion at the channel outlet is 94.2% and for this reason $T_{w,1}$ and $T_{gas-m,1}$ are different than T_{ad}. It is evident from the simulation of Case 1 that adiabatic operation with infinitely-fast catalytic chemistry leads to a substantial wall temperature superadiabaticity, particularly close to the channel entry ($x = 0$), which is detrimental to the catalyst and reactor integrity. Case 2 is computed with the detailed catalytic (C) reaction mechanism (Deutschmann et al., 2000) without inclusion of gaseous chemistry, while Case 3 is computed with the detailed catalytic and gas-phase (C+G) reaction mechanisms of Section 3.1 (Burke et al., 2012; Deutschmann et al., 2000). In addition, the model for Cases 2 and 3 includes heat conduction inside the solid platinum wall. The outer tubular channel surfaces are again adiabatic, as shown in the inset of Fig. 7. The plotted wall temperatures $T_{w,2}$ and $T_{w,3}$ in Fig. 7 refer to the inside wall surfaces (at the gas-wall interface, $r = R$); the radial temperature variation inside the solid is typically less than 10 K.

The wall temperature $T_{w,2}$ is lower than $T_{w,1}$ over most of the channel length due to the combined effects of finite-rate catalytic chemistry and redistribution of energy inside the channel via solid heat conduction ($\lambda_s = 96$ W m^{-1} K^{-1}, thermal conductivity of platinum at 1900 K). The maximum wall temperature is $T_{w,max,2} = 1941.7$ K which, although appreciably lower than $T_{w,max,1} = 2502$ K, is still 513.2 K above the adiabatic equilibrium temperature. Due to the solid heat conduction that redistributes energy in the channel, $T_{w,2}$ exceeds $T_{w,1}$ for $x > 27.5$ mm. Moreover, finite rate chemistry also leads to a lower mean gas temperature $T_{gas-m,2}$. The conversion of hydrogen at the reactor outlet is 91.8% for Case 2.

Case 3 with both surface and gas phase chemistry yields the lowest wall temperatures $T_{w,3}$ with a peak value $T_{w,max,3} = 1913.6$ K, which is 28.1 K lower than $T_{w,max,2}$. Moreover, $T_{w,3}$ is noticeably lower than $T_{w,2}$ over the length $x > 10$ mm (by up to 170 K) but still above the adiabatic equilibrium temperature T_{ad}. The significant suppression of the superadiabatic wall temperatures due to the presence of gaseous combustion was initially observed experimentally (Appel et al., 2005; Appel et al., 2002a) and then verified numerically (Ghermay et al., 2010; Mantzaras· 2008). Reason for this suppression is that gaseous combustion is confined close to the channel wall and thus "shields" the catalyst surface from the hydrogen-rich channel core. This in turn deprives hydrogen from the heterogeneous reaction pathway and thus moderates the catalytically-induced superadiabatic surface temperatures. On the other hand, gas-phase reactions lead to mean gas temperatures $T_{gas-m,3}$ higher that the corresponding values of Cases 1 and 2, and further result in increased hydrogen conversion (99.9% at the channel outlet for Case 3). The simulation of Case 2 illustrates that finite-rate surface chemistry reduces the degree of surface super-adiabaticity and, in conjunction with the heat conduction in the solid, results in more uniform surface temperatures. On the other hand, the simulation of Case 3 indicates that the presence of gaseous chemistry, while reducing the maximum superadiabatic surface temperature, leads to larger spatial non-uniformities of the surface temperature compared to Case 2.

Additional 2D simulations with higher inlet velocities $U_{IN} = 25$ and 35 m/s are carried out using detailed catalytic chemistry alone (no gas-phase chemistry), heat conduction in the solid wall and adiabatic outer walls. Similar to Fig. 7, the wall temperatures in Fig. 8 refer to the gas-wall interface at $r = R$. As seen in Fig. 8, increasing U_{IN} leads to roughly the same peak wall temperatures $T_{w,max}$ but the location of the peak wall temperatures, $x_{Tw,max}$, shifts downstream due to the elongated light-off lengths with increasing linear velocity. Moreover, an increase in U_{IN} renders the wall temperatures more uniform over the lengths $x > x_{Tw,max}$ whereas it increases the temperature non-uniformity over $x < x_{Tw,max}$; the former is due to the increased hydrogen slip with rising U_{IN} that "stretches" axially the wall temperature profiles, while the latter is a result of the elongated light-off distance with rising U_{IN}.

Given the cardinal requirement of increased surface temperature uniformity in the present hybrid microreactor application, the advantages of higher inflow velocities are evident. The channel attains higher surface temperature uniformity with increasing U_{IN}, except for the initial few millimeters (Fig. 8). An increase in U_{IN}, however, leads to higher hydrogen slips (the hydrogen conversions are 91.8%, 75.7% and 63.5% for $U_{IN} = 15$, 25 and 35 m/s, respectively). Nonetheless, this is not an overriding issue since many microreactors of the type shown in Fig. 2 can eventually be clustered in the concept of Fig. 1 such that the outflow of one microreactor can feed the next one in a recuperative operation. An additional advantage of the increased velocity (not evident in the adiabatic simulations of Fig. 8) is that higher mass throughputs
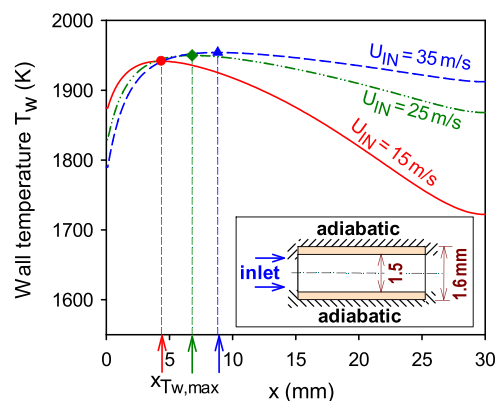

Fig. 8. Computed wall temperature profiles in a Pt-coated cylindrical channel with 30 mm length, 1.5 mm internal diameter and 1.6 mm outside diameter (geometry shown in the inset), at three different inlet flow velocities. Symbols indicate the maximum wall temperatures and arrows marked $x_{Tw,max}$ their corresponding axial locations. H$_2$/air catalytic combustion, $\varphi = 0.40$, $T_{IN} = 300$ K, $p = 1$ bar, only catalytic reactions included.

and hence higher chemical powers would lead to higher surface temperatures under strongly non-adiabatic operation as will be shown in the forthcoming Section 4.4. Finally, apart from increasing the inlet velocity, another strategy for obtaining more uniform surface temperatures can be inferred from Figs. 7 and 8. Since the diffusional imbalance of hydrogen always leads to channel wall temperatures dropping with increasing axial distance (at least over most of the channel length), a counterflow arrangement in adjacent channels can be pursued to increase the surface temperature uniformity.

4.2. Impact of gas phase reactions and selection of channel diameter

As discussed in the context of Fig. 7 (Cases 2 and 3), the presence of gaseous chemistry lowers the surface temperatures and increases the mean gas temperatures, and this is detrimental for the present application where high surface temperatures are desired. The impact of gaseous combustion is primarily controlled by two factors: wall temperature and surface to volume ratio (i.e. channel diameter), with the residence time playing a secondary role. Ghermay et al. (2011) have shown that, for atmospheric pressure and inlet temperature $T_{IN} = 293$ K, gas-phase combustion in fuel-lean H$_2$/air hetero-/homogeneous combustion is significant (contributes at least 5% to the total hydrogen conversion) only for wall temperatures in excess of 1550 K for 1-mm-diameter channels and in excess of 1350 K for 2-mm-diameter channels. For the present 1.5-mm-diameter channel, new simulations are reported below.
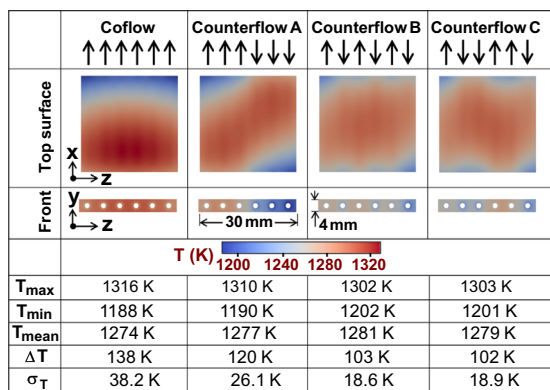
Two-dimensional channel computations are herein carried out to address the influence of wall temperature and channel diameter on gaseous combustion. The detailed heterogeneous and homogeneous reaction mechanisms of Section 3.1 are used, while the wall temperature is taken constant and is varied from 1300 to 1600 K. The employed parameters are $U_{IN} = 15$ m/s, $T_{IN} = 300$ K, $p = 1$ bar and $\varphi = 0.40$. The gaseous hydrogen conversion (as percentage of the total catalytic and gas-phase conversion) is plotted in Fig. 9 as a function of channel diameter (in the range 1.0–5.0 mm) at different wall temperatures.

Forthcoming simulations in Section 4.4 show that the maximum attained surface temperature is $T_w = 1326$ K. Predictions for $T_w = 1326$ K in Fig. 9 indicate that a 1.5-mm-diameter channel ensures a gaseous hydrogen conversion of only 0.3% (in actuality it is even less than 0.3% since the 1326 K value refers to the peak
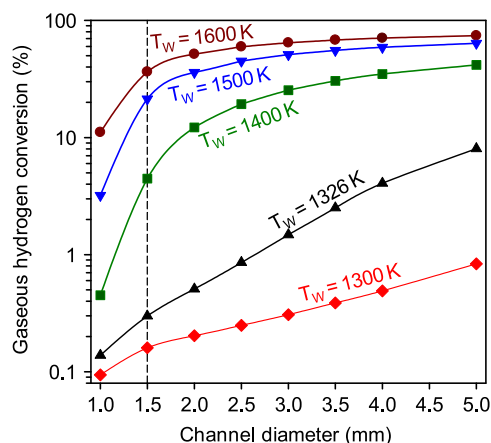
Fig. 9. Computed contribution of gaseous chemistry to the total hydrogen conversion (catalytic and gaseous) in a Pt-coated cylindrical channel a length of 30 mm, as a function of the channel diameter. The channel surface temperature is prescribed and varies from 1300 K to 1600 K. H_2/air catalytic combustion with $\varphi=0.40$, $T_{IN}=300$ K, $U_{IN}=15$ m/s, $p=1$ bar.
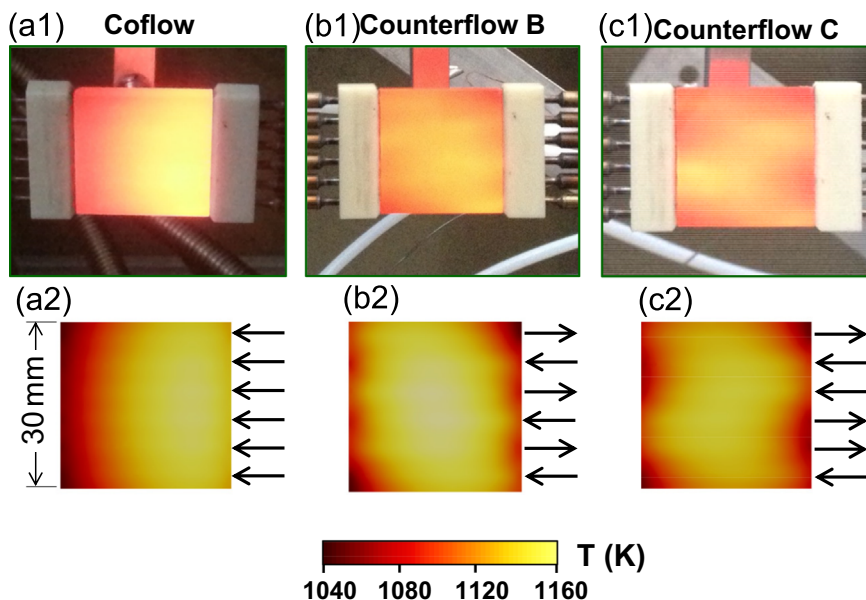

	Coflow ↑↑↑↑↑↑	Counterflow A ↑↑↑↓↓↓	Counterflow B ↑↓↑↓↑↓	Counterflow C ↑↓↓↑↑↓
T_{max}	1316 K	1310 K	1302 K	1303 K
T_{min}	1188 K	1190 K	1202 K	1201 K
T_{mean}	1274 K	1277 K	1281 K	1279 K
ΔT	138 K	120 K	103 K	102 K
σ_T	38.2 K	26.1 K	18.6 K	18.9 K

Fig. 10. Computed temperature distributions for four different channel-flow arrangements, one coflow and three counterflow (flow directions in each channel are denoted by arrows). H_2/air catalytic combustion with $\varphi=0.50$, $T_{IN}=300$ K, $U_{IN}=50$ m/s, $p=1$ bar. The maximum and minimum temperatures T_{max} and T_{min}, respectively, their difference ΔT, the mean temperature and the standard deviation σ on the top surface are also given.

predicted surface temperature). Consequently, the 1.5 mm channel diameter was selected in the present reactor design to mitigate gaseous combustion.

4.3. Optimization of channel flow configuration

Four different channel-flow configurations are simulated, the coflow and three counterflow ones (termed A, B and C, the flow directions are shown in Fig. 10). Predicted top and front reactor surface temperature distributions for the four flow configurations are illustrated in Fig. 10 for a case with $\varphi=0.50$ and $U_{IN}=50$ m/s. The maximum and minimum temperatures T_{max} and T_{min}, respectively, their difference ΔT, the mean temperature T_{mean} and the standard deviation σ_T of the top surface are also given in Fig. 10. The counterflow configurations provide modestly higher mean temperatures (by 3-7 K) compared to the coflow $T_{mean}=1274$ K but, most importantly, higher spatial temperature uniformities as manifested by their lower ΔT and σ_T. In particular, the counterflow configurations B and C yield temperature differences ΔT of 103 K and 102 K, respectively. The coflow configuration in Fig. 10 yields the highest peak surface temperature, $T_{max}=1326$ K, occurring at the front part of the reactor (in agreement with the foregoing single-channel simulations of Fig. 7). However, this is accompanied by a significant temperature drop at the reactor rear, with a resulting larger $\Delta T=138$ K, again in agreement with the findings in Section 4.1 and Fig. 7. Note that the $\Delta T=138$ K of the coflow case is still modest because of the very high velocity $U_{IN}=50$ m/s in Fig. 10, which moderates the temperature differences along the streamwise direction as discussed previously in the context of Fig. 8. Due to the strong external heat losses, the peak temperatures in all configurations of Fig. 10 are underadiabatic ($T_{ad}=1646.7$ K). The advantage of the counterflow configurations in attaining better temperature uniformity is clearly evident. Experiments at various configurations are subsequently performed.

Visual inspection of patterns formed on the reactor's top surface during operation readily identifies the particular flow configurations. This is shown in Fig. 11, whereby photographs of the top surface taken with a conventional camera are compared with simulated 2D temperature distributions for the coflow, counterflow B and counterflow C configurations ($\varphi=0.40$ and $U_{IN}=35$ m/s). Best

Fig. 11. Photographs (a1, b1, c1) and simulations (a2, b2, c2) of top surface temperature distributions for the coflow and the counterflow B and C configurations. H_2/air catalytic combustion with $\varphi=0.40$, $T_{IN}=300$ K, $U_{IN}=35$ m/s.
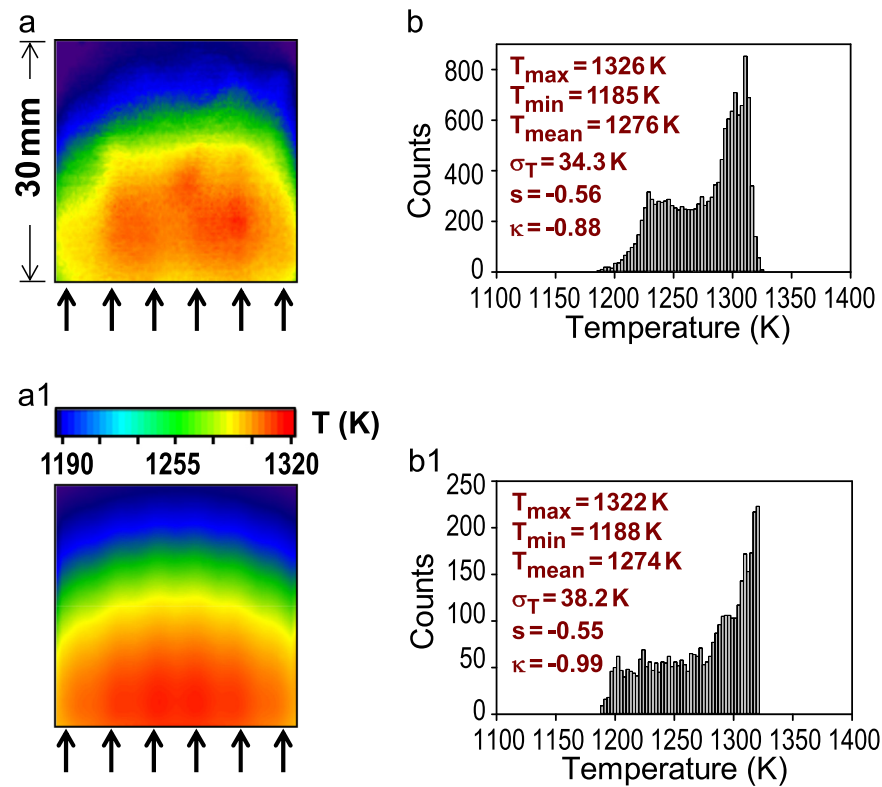
Fig. 12. Measured (a, b) and predicted (a1, b1) temperature distributions for the coflow configuration, $\varphi=0.50$ and $U_{IN}=50$ m/s. Temperature contour maps (a, a1) and histograms (b, b1); σ_T, s and κ denote the standard deviation, skewness and kurtosis, respectively, of the distributions.
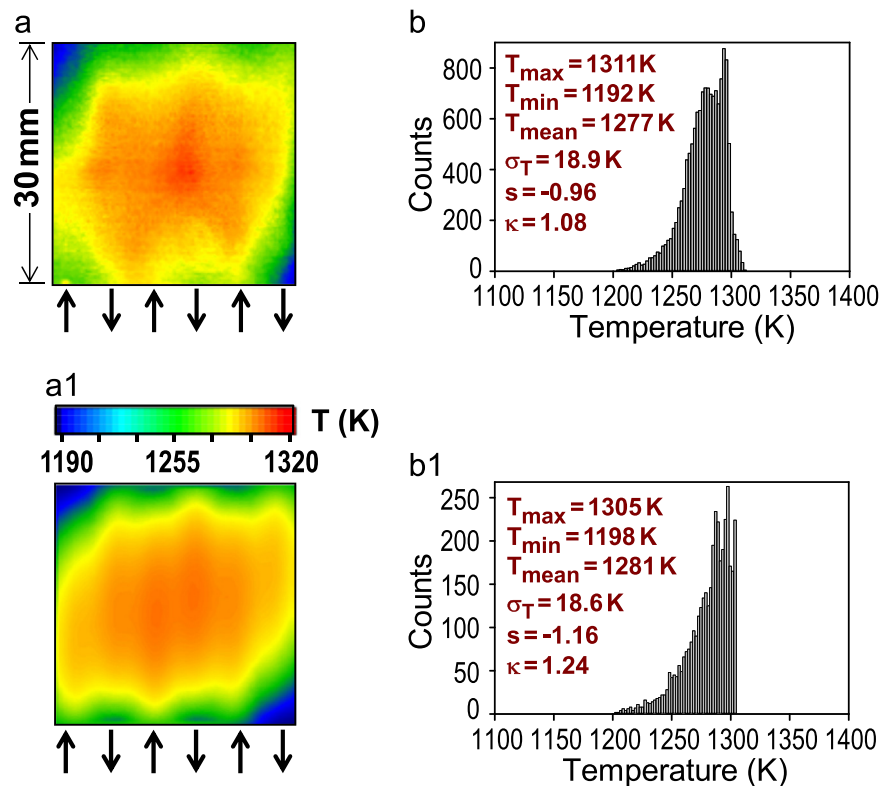
Fig. 13. Measured (a, b) and predicted (a1, b1) temperature distributions for the counterflow B configuration, $\varphi=0.50$ and $U_{IN}=50$ m/s. Temperature contour maps (a, a1) and histograms (b, b1); σ_T, s and κ denote the standard deviation, skewness and kurtosis, respectively, of the distributions.

temperature uniformity is obtained with the counterflow B and C cases (see Fig. 10, nearly equal performance). In the following, experiments will be carried out in counterflow B, which is selected over counterflow C due to its slightly higher mean temperature. For comparison purposes, the coflow configuration will also be examined.

a

b
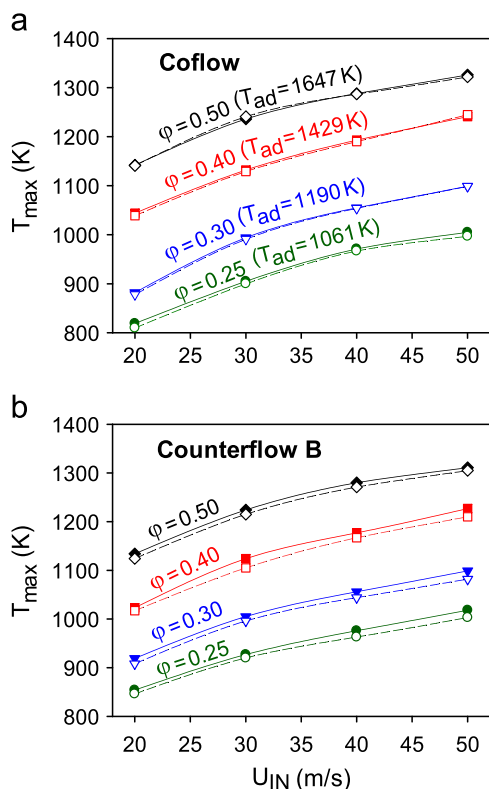
Fig. 14. Measured (solid lines) and predicted (dashed lines) maximum top-surface temperatures as a function of inlet velocity U_{IN} at various equivalence ratios φ: (a) Coflow, and (b) Counterflow B configuration. T_{ad} denote the adiabatic equilibrium temperatures of the incoming reactants.

4.4. Comparison of measurements and predictions

Experiments are performed by varying the inlet velocities U_{IN} in the range 15–50 m/s (at increments of 5 m/s), and the H_2/air equivalence ratios φ in the range 0.25–0.50 (at increments of 0.05). Measured and predicted 2D temperature contour maps and histograms of the top reactor surface are illustrated in Fig. 12 for the coflow configuration and in Fig. 13 for the counterflow B configuration, both at $\varphi = 0.50$ and $U_{IN} = 0.50$ m/s. The agreement between measurements and predictions is quite good, not only in the mean temperatures (T_{mean}) and standard deviations (σ_T) but also in higher distribution moments, as shown by the provided values of skewness s and kurtosis κ in Fig. 12(b, b1) and Fig. 13(b, b1)).

Measured and predicted maximum top surface temperatures are shown in Fig. 14 for the two investigated flow configurations, at selected φ and U_{IN}. For a given φ, a rise in U_{IN} leads to higher maximum surface temperatures since the enhanced mass throughput leads to an increase in heat generation on the catalytic surface. Moreover, with decreasing equivalence ratio the differences between maximum surface temperatures and the corresponding adiabatic equilibrium temperatures T_{ad} diminish (T_{ad} of the four equivalence ratios are provided in Fig. 14a). Characteristically, for the coflow arrangement in Fig. 14a and for $U_{IN} = 50$ m/s, the measured maximum surface temperatures T_{max} are lower than T_{ad} by 321 K ($\varphi = 0.50$) and by 56 K ($\varphi = 0.25$); for $U_{IN} = 20$ m/s the corresponding differences are 505 K and 242 K. The same trends are also observed for the counterflow arrangement in Fig. 14b.

Comparisons between measured and predicted maxima, minima and standard deviations of the top surface temperatures are summarized in Table 2 for the two flow configurations. The agreement between measurements and predictions is fairly good (0–19 K for T_{max}, 1–27 K for T_{min}, and 0–4.3 K for σ_T). Predicted and

Table 2
Comparisons of measured and predicted top surface temperatures[a].

U_{IN} (m/s) φ	20	30	40	50
0.25	**Coflow**	**Coflow**	**Coflow**	**Coflow**
	T_{max}: 819 K (*810*)	T_{max}: 905 K (*900*)	T_{max}: 971 K (*967*)	T_{max}: 1005 K (*997*)
	T_{min}: 763 K (*778*)	T_{min}: 841 K (*853*)	T_{min}: 897 K (*915*)	T_{min}: 926 K (*940*)
	σ_T: 11.2 K (*9.8*)	σ_T: 13.2 K (*14.1*)	σ_T: 15.8 K (*15.3*)	σ_T: 16.8 K (*17.0*)
	Counterflow B	**Counterflow B**	**Counterflow B**	**Counterflow B**
	T_{max}: 854 K (*846*)	T_{max}: 927 K (*920*)	T_{max}: 976 K (*963*)	T_{max}: 1018 K (*1003*)
	T_{min}: 811 K (*819*)	T_{min}: 875 K (*882*)	T_{min}: 913 K (*921*)	T_{min}: 942 K (*953*)
	σ_T: 6.4 K (*5.9*)	σ_T: 7.8 K (*7.8*)	σ_T: 9.2 K (*8.7*)	σ_T: 10.4 K (*9.9*)
0.30	**Coflow**	**Coflow**	**Coflow**	**Coflow**
	T_{max}: 882 K (*878*)	T_{max}: 994 K (*991*)	T_{max}: 1051 K (*1054*)	T_{max}: 1099 K (*1099*)
	T_{min}: 812 K (*832*)	T_{min}: 912 K (*924*)	T_{min}: 961 K (*988*)	T_{min}: 995 K (*1018*)
	σ_T: 14.5 K (*14.5*)	σ_T: 18.5 K (*20.1*)	σ_T: 21.0 K (*19.9*)	σ_T: 22.7 K (*24.3*)
	Counterflow B	**Counterflow B**	**Counterflow B**	**Counterflow B**
	T_{max}: 919 K (*908*)	T_{max}: 1005 K (*996*)	T_{max}: 1056 K (*1044*)	T_{max}: 1099 K (*1082*)
	T_{min}: 869 K (*872*)	T_{min}: 945 K (*950*)	T_{min}: 978 K (*988*)	T_{min}: 1019 K (*1017*)
	σ_T: 7.6 K (*7.3*)	σ_T: 9.2 K (*9.0*)	σ_T: 11.5 K (*10.4*)	σ_T: 12.5 K (*11.7*)
0.40	**Coflow**	**Coflow**	**Coflow**	**Coflow**
	T_{max}: 1044 K (*1039*)	T_{max}: 1132 K (*1129*)	T_{max}: 1193 K (*1190*)	T_{max}: 1241 K (*1245*)
	T_{min}: 935 K (*951*)	T_{min}: 1007 K (*1030*)	T_{min}: 1048 K (*1072*)	T_{min}: 1097 K (*1124*)
	σ_T: 26.6 K (*27.1*)	σ_T: 28.8 K (*30.1*)	σ_T: 32.0 K (*35.2*)	σ_T: 33.3 K (*36.4*)
	Counterflow B	**Counterflow B**	**Counterflow B**	**Counterflow B**
	T_{max}: 1023 K (*1017*)	T_{max}: 1124 K (*1105*)	T_{max}: 1177 K (*1167*)	T_{max}: 1227 K (*1210*)
	T_{min}: 959 K (*958*)	T_{min}: 1040 K (*1035*)	T_{min}: 1078 K (*1083*)	T_{min}: 1121 K (*1111*)
	σ_T: 10.2 K (*10.1*)	σ_T: 13.3 K (*12.4*)	σ_T: 15.2 K (*14.6*)	σ_T: 16.9 K (*16.6*)
0.50	**Coflow**	**Coflow**	**Coflow**	**Coflow**
	T_{max}: 1142 K (*1141*)	T_{max}: 1236 K (*1241*)	T_{max}: 1288 K (*1287*)	T_{max}: 1326 K (*1326*)
	T_{min}: 1002 K (*1017*)	T_{min}: 1088 K (*1113*)	T_{min}: 1136 K (*1155*)	T_{min}: 1185 K (*1188*)
	σ_T: 34.7 K (*37.6*)	σ_T: 34.3 K (*38.6*)	σ_T: 34.2 K (*38.1*)	σ_T: 34.3 K (*38.2*)
	Counterflow B	**Counterflow B**	**Counterflow B**	**Counterflow B**
	T_{max}: 1134 K (*1124*)	T_{max}: 1224 K (*1215*)	T_{max}: 1280 K (*1271*)	T_{max}: 1311 K (*1305*)
	T_{min}: 1044 K (1054)	T_{min}: 1118 K (*1133*)	T_{min}: 1158 K (*1171*)	T_{min}: 1192 K (*1202*)
	σ_T: 13.1 K (*11.9*)	σ_T: 15.8 K (*15.3*)	σ_T: 18.1 K (*18.3*)	σ_T: 18.9 K (*18.6*)

[a] Maximum (T_{max}), minimum (T_{min}) and standard deviations (σ_T) of top surface temperatures. First values are measurements, values in parentheses are predictions.
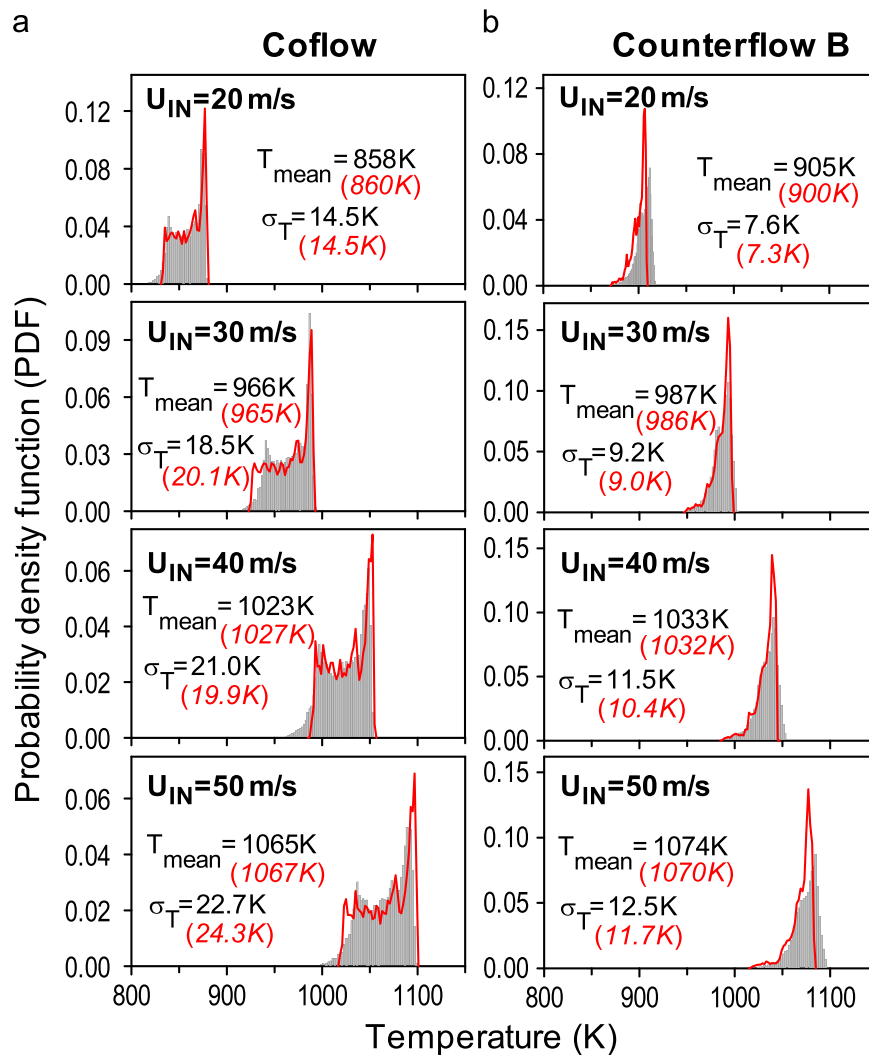
Fig. 15. Measured (gray areas) and predicted (solid lines) temperature PDFs of the top reactor surface at various inlet velocities U_{IN} and $\varphi=0.30$: (a) coflow and (b) counterflow B configuration. Measured and predicted (the latter in parentheses) mean temperatures T_{mean} and standard deviations σ_T are also given.

measured probability density functions (PDFs) of top-surface temperatures for the two flow configurations are plotted in Fig. 15 for a fixed equivalence ratio $\varphi=0.30$ and various flow velocities. Similar PDFs are illustrated in Fig. 16 for a fixed velocity $U_{IN}=30$ m/s and various equivalence ratios. Measured and predicted PDF shapes are again in good agreement with each other. The PDFs become broader with increasing either U_{IN} (Fig. 15) or φ (Fig. 16), as manifested by the rise of the corresponding standard deviations. Moreover, the PDFs of the counterflow B configuration are closer to symmetric (with a skew towards the lower temperatures), while the PDFs of the coflow configuration have a consistent bimodal shape with two distinct peaks at the high and low temperature regions. Such detailed comparisons of temperature distributions have not been elaborated in past studies.

The in-channel combustion processes are finally discussed using the simulation results. Predicted hydrogen conversions for the two flow configurations are shown in Fig. 17. As discussed in Section 4.1, a continuous increase of the inlet velocity results in increased hydrogen slip. For the coflow configuration, hydrogen conversions range from 52.5% to 78.5% for $\varphi=0.50$ and from 47.6 to 70.8% for $\varphi=0.25$. The counterflow B configuration leads to slightly higher conversions: 52.6–79.1% for $\varphi=0.50$ and from 48.0 to 71.2% for $\varphi=0.25$.

The dependence of hydrogen conversion on equivalence ratio is noticeable and it is mainly attributed to the higher wall

temperatures at larger φ, which in turn accelerate the catalytic reactions. This is because the conversion of hydrogen is not transport-limited but mixed kinetic/transport controlled at the present operating conditions. Despite the high reactivity of hydrogen on platinum, the employed large velocities result in visible finite-rate chemistry effects. This is shown in Fig. 18, wherein radial profiles of hydrogen mass fraction are plotted for the counterflow B configuration at five selected axial positions. The plots in Fig. 18 refer to the second channel of the microreactor (located at $z=7.5$ mm in Fig. 3); however, qualitatively similar results are obtained for other channels and/or for different (coflow) configuration.

A measure of finite-rate chemistry (or equivalently departure from transport-limited operation) is the ratio of the hydrogen mass fraction at the wall to the corresponding centerline value, $Y_{H2}(x, r=\pm R)/Y_{H2}(x, r=0)$. This ratio is identically zero for infinitely-fast chemistry (i.e. transport-limited hydrogen conversion), while the effects of finite-rate chemistry become appreciable when it exceeds a typical value of $\sim5\%$. In Fig. 18a ($U_{IN}=20$ m/s, $\varphi=0.25$) the aforementioned ratio varies from 14.9% to 8.8%, while in Fig. 18b ($U_{IN}=20$ m/s, $\varphi=0.50$) from 20.1% to 2.0%, with the highest values referring to $x=1$ mm. It is worth noting that finite-rate chemistry effects at $x=1$ mm are more pronounced at the richer stoichiometry $\varphi=0.50$ than at the leaner $\varphi=0.25$: in the former case the ratio $Y_{H2}(x=1$ mm, $r=0.75$ mm$)/Y_{H2}(x=1$ mm, $r=0)$ is 20.1% while
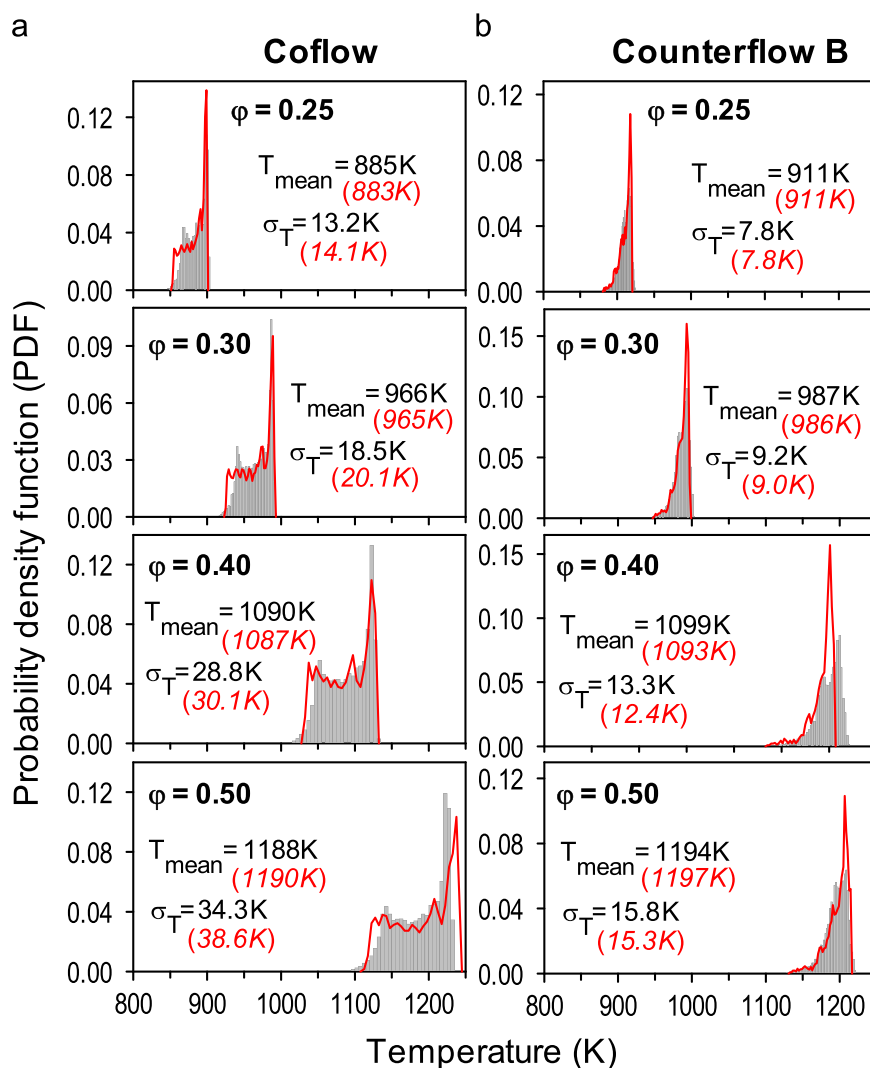
Fig. 16. Measured (gray areas) and predicted (solid lines) temperature PDFs of the top reactor surface at various equivalence ratios φ and $U_{IN} = 30$ m/s: (a) coflow and (b) counterflow B configuration. Measured and predicted (the latter in parentheses) mean temperatures T_{mean} and standard deviations σ_T are also given.

in the latter it is 14.9%. This is a result of the well-known self-inhibition of hydrogen catalytic ignition (Behrendt et al., 1996; Michelon et al., 2015), whereby leaner mixtures ignite easier than richer ones. Finally, in Fig. 18c ($U_{IN} = 50$ m/s, $\varphi = 0.50$) the wall-to-centerline hydrogen mass fraction ratio ranges from 28.0% to 3.1%. The more pronounced finite-rate chemistry effects in Fig. 18c at $x = 1$ mm compared to Fig. 18b are due to the higher inlet velocity. All in all, finite-rate chemistry effects are appreciable in the microreactor under investigation and exemplify the importance of a detailed surface kinetic scheme in the numerical model.

4.5. Radiation efficiency

Of prime interest in this work is the radiation efficiency, i.e. the efficient conversion of the chemical and thermal energy in the catalytic channels into radiation energy. In the following, the radiation efficiency is defined as:

$$\eta_{rad} = \frac{Q_{rad}}{\sum\limits_{i=1}^{6} \dot{m}_i \ (h_{i,IN} - h_{i,OUT})} \tag{23}$$

with $h_{i,IN}$ and $h_{i,OUT}$ the inlet and outlet enthalpies of the gas mixture and $\dot{m}_i$ the mass flow rate in the i-th channel ($\dot{m}_i$ is the same for all six channels). In Eq. (23) the enthalpy difference and not the

inlet enthalpy is used, since many microreactors will be eventually clustered together in a recuperative way. The total radiation power Q_{rad} in Eq. (23) is:

$$Q_{rad} = \int_A \varepsilon\sigma\left(T_w^4 - T_\infty^4\right) dA, \tag{24}$$

where the area A in the integral refers to the four radiating surfaces of the microreactor. Typically the top 30×30 mm^2 surface accounts for 32-44% of the total radiating power, depending on the operating conditions. The radiation powers Q_{rad} are shown in Fig. 19 for the two flow configurations and for various equivalence ratios as a function of inlet velocity. The radiation power increases with increasing either the flow velocity or the equivalence ratio, due the accompanying increase in surface temperatures. For the coflow configuration, Q_{rad} is in the range 103-196 W for $\varphi = 0.50$ and 28-64 W for $\varphi = 0.25$. The counterflow B configuration leads to higher Q_{rad} (109–200 W for $\varphi = 0.50$ and 34-69 W for $\varphi = 0.25$) since its temperature distributions have higher mean values and reduced populations at lower temperatures (see Figs. 15 and 16).

The radiation efficiencies η_{rad} for the two configurations are shown in Fig. 20. For the coflow configuration, η_{rad} is in the range 56.4–73.6% for $\varphi = 0.50$ and 33.7–57.2% for $\varphi = 0.25$. The counterflow B configuration leads to higher η_{rad} (63.3–76.2% for $\varphi = 0.50$ and 43.4–63.5% for $\varphi = 0.25$). The attained $\eta_{rad} > 70\%$ at large equivalence ratios and high velocities are of particular interest for the microreactor application in
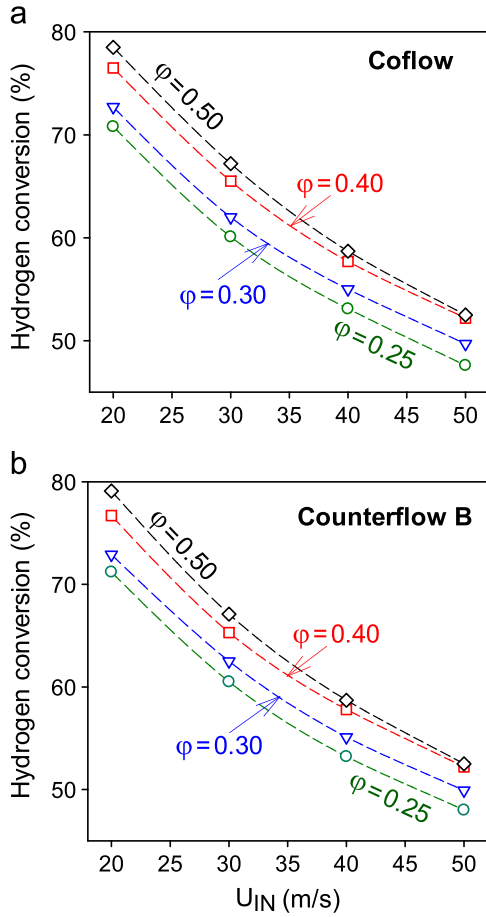
Fig. 17. Predicted hydrogen conversions as a function of inlet velocity U_{IN} at various equivalence ratios φ: (a) Coflow, and (b) Counterflow B configuration.
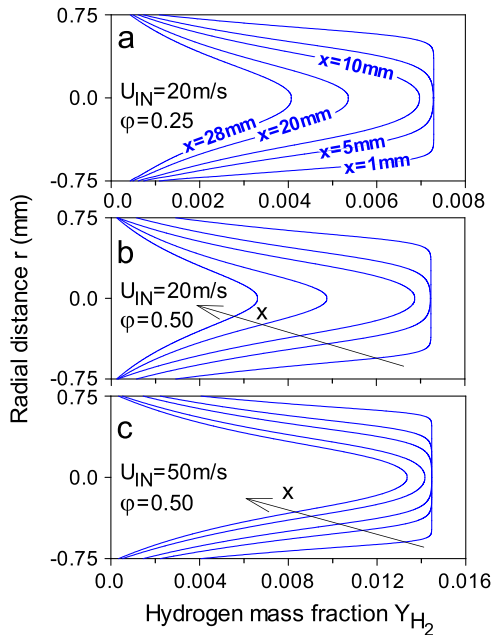
Fig. 18. Predicted radial profiles of hydrogen mass fraction in one catalytic channel of the reactor for the counterflow B configuration at five selected axial positions ($x=1$, 5, 10, 20 and 28 mm); (a) $U_{IN}=20$ m/s, $\varphi=0.25$, (b) $U_{IN}=20$ m/s, $\varphi=0.50$ and (c) $U_{IN}=50$ m/s, $\varphi=0.50$.
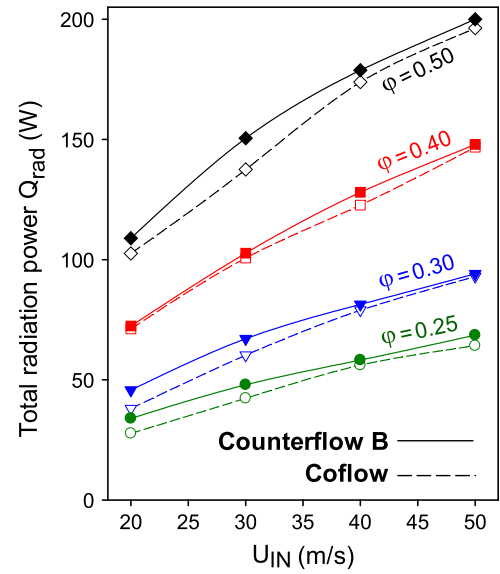
Fig. 19. Predicted total radiation power Q_{rad} as a function of inlet velocity U_{IN} for various equivalence ratios φ. Coflow configuration (dashed-lines, open symbols) and counterflow B configuration (solid lines, filled symbols).

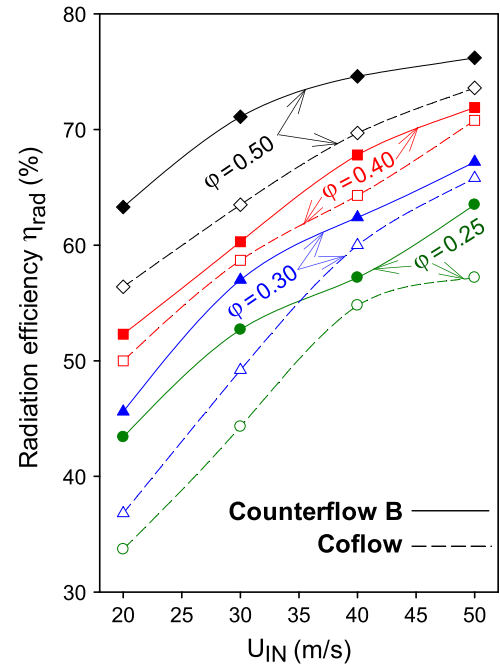Fig. 20. Radiation efficiency as a function of inlet velocity U_{IN} for various equivalence ratios φ. Coflow configuration (dashed-lines, open symbols) and counterflow B configuration (solid lines, filled symbols).

conjunction with TPVs. The remaining heat losses (100%-η_{rad}) are distributed among free convection heat losses and parasitic heat losses via conduction to the steel tubes and zirconia support (see Section 3.2). For $\eta_{rad} > 60\%$ the convection heat losses comprise 18-25% and the conduction heat losses 6–15% of the inlet/outlet gas enthalpy difference. On the other hand, for $\eta_{rad} < 45\%$ convection and conduction heat losses are roughly equal (the former account for 27-35% and the latter for 25-37% of the inlet/outlet gas enthalpy difference). When many microreactors of the type shown in Fig. 4 are clustered in a recuperative way, the parasitic conduction losses are expected to be

Nomenclature

A	radiating area of microreactor, Eq. (24)
C_k	concentration of k-th species, Eq. (10)
$c_{p,k}, c_p$	specific heat of k-th gaseous species, mixture specific heat, Eq. (5)
D_{km}	mixture-average diffusion coefficient of k-th gaseous species, Eq. (13)
D_k^T	species thermal diffusion coefficient, Eq. (13)
h	external convective heat transfer coefficient, Eq. (17)
$h_{i,IN}, h_{i,OUT}$	enthalpies of gas mixture in i-th channel at inlet and outlet, Eq. (23)
H	reactor height, Fig. 3a
K_g, K_s	number of gaseous and surface species, Eqs. (5) and (9)
k, m	indices for gas-phase and surface species, respectively
L	channel and reactor length, Fig. 3a
Le_{H2}	Lewis number of hydrogen (thermal over mass diffusivity), Eq. (18)
N_s	number of surface reactions, Eq. (10)
p	pressure
Q_{rad}	radiation power, Eq. (24)
r	radial coordinate of channel
R	channel radius, Fig. 3a
R^0	universal gas constant, Eq. (6)
$\dot{s}_m, \dot{s}_k$	heterogeneous molar production rate of m-th surface species and k-th gaseous species, Eqs. (10) and (8)
s	skewness of temperature distribution, Figs. 12 and 13
T, T_∞	temperature, ambient temperature
T_{ad}	adiabatic equilibrium temperature, Eq. (19)
u, U_{IN}	streamwise velocity component, inlet streamwise velocity
ν	transverse velocity component

$W_k, \overline{W}$	molecular weight of k-th gaseous species, mixture molecular weight
W	reactor width, Fig. 3a
Y_k	mass fraction of k-th gaseous species
x, y, z	streamwise, transverse and lateral reactor coordinates, Fig. 3a

Greek Symbols

Γ	surface site density, Eq. (9)
ε	surface emissivity, Eq. (17)
$\varepsilon_{i\ell}$	parameters in surface reaction rate coefficient, Eq. (11)
η_{rad}	radiation efficiency, Eq. (23)
θ_m	coverage of m-th surface species, Eq. (11)
κ	kurtosis of temperature distribution, Figs. 12 and 13
λ_g	thermal conductivity of gas, Eqs. (5) and (16)
λ_s	thermal conductivity of solid, Eqs. (15) and (16)
μ	dynamic viscosity of gas, Eq. (2)
$\mu_{i\ell}$	parameters in surface reaction rate coefficient, Eq. (11)
ρ	density of gas, Eqs. (1)-(5)
σ	Stefan-Boltzmann constant, Eq. (17)
σ_T	standard deviation of temperature distribution, Figs. 12, 13, 15, 16
σ_m	site occupancy of m-th surface species, Eq. (9)
φ	fuel-to-air equivalence ratio
$\dot{\omega}_k$	homogeneous molar production rate of k-th gaseous species, Eq. (5)

Subscripts

IN, OUT	inlet, outlet
r	radial
w	wall

significantly reduced.

5. Conclusions

The catalytic combustion of fuel-lean H_2/air mixtures has been investigated experimentally and numerically in a $30 \times 30 \times 4$ mm^3 ceramic (SiC) microreactor, which is equipped with six 1.5-mm ID platinum tubes. Application of the microreactor in power generation systems, in conjunction with a thermoelectric device, requires high and spatially uniform surface temperatures. Three-dimensional simulations with conjugate heat transfer, appropriate external heat losses and detailed catalytic and gas-phase chemistry are used to optimize the channel flow configurations. Experiments are performed for various fuel-to-air stoichiometries (0.25–0.50) and mass throughputs (inlet channel velocities 15–50 m/s) at coflow and counterflow channel configurations, and involve measurements of the microreactor top-surface temperatures with an IR camera. The following are the key conclusions of this study.

1) The diffusional imbalance of hydrogen leads to large temperature non-uniformities along the catalytic channel walls during catalytic combustion of fuel-lean H_2/air mixtures. Moreover, under adiabatic operation, the front section of the catalytic channel experiences superadiabatic surface temperatures. Operation at higher mass throughputs (leading to hydrogen slip) reduces the temperature spatial non-uniformities. The onset of gaseous combustion lowers the catalyst surface temperatures and is thus detrimental for power generation applications. It is shown that the selected platinum tube diameter of 1.5 mm mitigates the contribution of gaseous combustion,

allowing for higher wall temperatures and hence to more efficient heat transfer towards the external microreactor surfaces.

2) Four different channel configurations are tested for optimum temperature uniformity. Counterflow configurations are shown superior to the coflow configuration in attaining good surface temperature uniformities with differences between maximum and minimum surface temperatures of about 100 K and standard deviations of surface temperatures less than 19 K for a specific counterflow arrangement.

3) Maximum measured surface temperatures increase with rising mass throughput (inlet velocity) and equivalence ratio. For $U_{IN}=50$ m/s and $\varphi=0.50$, the maximum attained surface temperature is 1326 K for the coflow and 1311 K for the counterflow configuration, with corresponding standard deviations of 38.2 and 18.6 K. Such temperatures are key to efficient operation of the microreactor in conjunction with TPV modules.

4) The in-channel combustion processes are analyzed using the simulations. It is shown that the catalytic conversion of hydrogen is not transport-limited, with ratios of wall-to-centerline hydrogen mass fractions exceeding at certain axial positions 15%. This exemplifies the importance of accurate surface reaction mechanisms in the numerical simulations. For the investigated counterflow configuration, the hydrogen conversions are in the range 52.6–79.1% for $\varphi=0.50$ and 48.0–71.2% for $\varphi=0.25$.

5) Comparisons between measurements and predictions are very favorable not only in terms of mean temperatures but also in terms of temperature PDF shapes and higher distribution moments. The investigated counterflow configuration yields narrower PDFs

slightly skewed to the low temperatures, while the coflow config-
uration yields distributions approaching bimodal shapes.

6) Computed radiation efficiencies, based on the enthalpy dif-
ference between reactants and products, increase with increasing
inlet velocity and equivalence ratio and fall in the range 63.3–76.2%
for $\varphi = 0.50$ and the counterflow configuration.

Acknowledgments

References

Ahn, J.M., Eastwood, C., Sitzki, L., Ronney, P.D., 2005. Gas-phase and catalytic
combustion in heat-recirculating burners. Proc. Combust. Inst. 30, 2463–2472.
Appel, C., Mantzaras, J., Schaeren, R., Bombach, R., Inauen, A., 2005. Turbulent
catalytically stabilized combustion of hydrogen/air mixtures in entry channel
flows. Combust. Flame 140, 70–92.
Appel, C., Mantzaras, J., Schaeren, R., Bombach, R., Inauen, A., Kaeppeli, B., Hem-
merling, B., Stampanoni, A., 2002a. An experimental and numerical investiga-
tion of homogeneous ignition in catalytically stabilized combustion of hydro-
gen/air mixtures over platinum. Combust. Flame 128, 340–368.
Appel, C., Mantzaras, J., Schaeren, R., Bombach, R., Kaeppeli, B., Inauen, A., 2002b.
An experimental and numerical investigation of turbulent catalytically stabi-
lized channel flow combustion of hydrogen/air mixtures over platinum. Proc.
Combust. Inst. 29, 1031–1038.
ASHRAE, 2009. Handbook-Fundamentals (SI Edition). American Society of Heating,
Refrigerating and Air-Conditioning Engineers, Inc.
Behrendt, F., Deutschmann, O., Schmidt, R., Warnatz, J., 1996. Ignition and extinc-
tion of hydrogen-air and methane-air mixtures over platinum and palladium.
In: Warren, B. (Ed.), Heterogeneous Hydrocarbon Oxidation. ACS Symposium
Series, Washington DC.
Brenan, K.E., Campbell, S.L., Petzold, L.R., 1989. Numerical Solution of Initial-Value
Problems in Differential-Algebraic Equations. Prentice Hall, New York.
Bui, P.A., Vlachos, D.G., Westmoreland, P.R., 1996. Homogeneous ignition of
hydrogen/air mixtures over platinum. Proc. Combust. Inst. 26, 1763–1770.
Burke, M.P., Chaos, M., Ju, Y., Dryer, F.L., Klippenstein, S.J., 2012. Comprehensive H_2/
O_2 kinetic model for high-pressure combustion. Int. J. Chem. Kinet. 44,
444–474.
Carroni, R., Griffin, T., 2010. Catalytic hybrid lean combustion for gas turbines. Catal.
Today 155, 2–12.
Casanovas, A., Saint-Gerons, M., Griffon, F., Llorca, J., 2008. Autothermal generation
of hydrogen from ethanol in a microreactor. Int. J. Hydrogen Energy 33,
1827–1833.
Coltrin, M.E., Kee, R.J., Rupley, F.M., 1996. Surface Chemkin: A Fortran package for
analyzing heterogeneous chemical kinetics at the solid surface-gas phase
interface, Report no. SAND90-8003C. Sandia National Laboratories, USA.
Deutschmann, O., Maier, L.I., Riedel, U., Stroemman, A.H., Dibble, R.W., 2000.
Hydrogen assisted catalytic combustion of methane on platinum. Catal. Today
59, 141–150.
Diehm, C., Deutschmann, O., 2014. Hydrogen production by catalytic partial oxi-
dation of methane over staged Pd/Rh coated monoliths: Spatially resolved
concentration and temperature profiles. Int. J. Hydrogen Energy 39,
17998–18004.
Donazzi, A., Pagani, D., Lucotti, A., Tommasini, M., Beretta, A., Groppi, G., Castiglioni,
C., Forzatti, P., 2014. Annular reactor testing and Raman surface characterization
in the CPO of methane and propylene. Appl. Catal. A-Gen. 474, 149–158.
Eriksson, S., Wolf, M., Schneider, A., Mantzaras, J., Raimondi, F., Boutonnet, M., Järas,
S., 2006. Fuel rich catalytic combustion of methane in zero emissions power
generation processes. Catal. Today 117, 447–453.
Evans, C.J., Kyritsis, D.C., 2009. Operational regimes of rich methane and propane/
oxygen flames in mesoscale non-adiabatic ducts. Proc. Combust. Inst. 32,
3107–3114.
Fan, A.W., Wan, J.L., Maruta, K., Nakamura, H., Yao, H., Liu, W., 2013. Flame dynamics
in a heated meso-scale radial channel. Proc. Combust. Inst. 34, 3351–3359.
Federici, J.A., Vlachos, D.G., 2011. Experimental studies on syngas catalytic com-
bustion on Pt/Al_2O_3 in a microreactor. Combust. Flame 158, 2540–2543.
Ghermay, Y., Mantzaras, J., Bombach, R., 2010. Effects of hydrogen preconversion on
the homogeneous ignition of fuel-lean H_2/O_2/N_2/CO_2 mixtures over platinum at
moderate pressures. Combust. Flame 157, 1942–1958.
Ghermay, Y., Mantzaras, J., Bombach, R., Boulouchos, K., 2011. Homogeneous
combustion of fuel lean H_2/O_2/N_2 mixtures over platinum at elevated pressures
and preheats. Combust. Flame 158, 1491–1506.
Hartmann, M., Maier, L., Minh, H.D., Deutschmann, O., 2010. Catalytic partial oxi-
dation of iso-octane over rhodium catalysts: an experimental, modeling, and
simulation study. Combust. Flame 157, 1771–1782.

Hettel, M., Diehm, C., Bonart, H., Deutschmann, O., 2015. Numerical simulation of a
structured catalytic methane reformer byDUO: The new computational inter-
face for OpenFOAM® and DETCHEMTM. Catal. Today 258, 230–240.
Holladay, J.D., Wang, Y., Jones, E., 2004. Review of developments in portable
hydrogen production using microreactor technology. Chem. Rev. 104,
4767–4789.
HRC-Power, 2015. Hybrid Renewable energy Converter for continuous and flexible
power production, ⟨http://cordis.europa.eu/project/rcn/105881_de.html⟩.
Jiang, B., Santis-Alvarez, A.J., Muralt, P., Poulikakos, D., Bohrani, N., Thome, J.R.,
Maeder, T., 2015. Design and packaging of a highly integrated microreactor
system for high-temperature on-board hydrogen production. Chem. Eng. J. 275,
206–219.
Kaisare, N.S., Lee, J.H., Fedorov, A.G., 2005. Operability analysis and design of a
reverse-flow microreactor for hydrogen generation via methane partial oxida-
tion. Ind. Eng. Chem. Res. 44, 8323–8333.
Kamijo, T., Suzuki, Y., Kasagi, N., Okamasa, T., 2009. High-temperature micro cata-
lytic combustor with Pd/nano-porous alumina. Proc. Combust. Inst. 32,
3019–3026.
Karagiannidis, S., Mantzaras, J., 2012. Numerical investigation on the hydrogen-
assisted start-up of methane-fueled, catalytic microreactors. Flow Turbul.
Combust. 89, 215–230.
Karagiannidis, S., Mantzaras, J., Boulouchos, K., 2011. Stability of hetero-/homo-
geneous combustion in propane and methane fueled catalytic microreactors:
channel confinement and molecular transport effects. Proc. Combust. Inst. 33,
3241–3249.
Kee, R.J., Dixon-Lewis, G., Warnatz, J., Coltrin, M.E., Miller, J.A., 1996a. A Fortran
computer code package for the evaluation of gas-phase multicomponent
transport properties, Report no. SAND86-8246. Sandia National Laboratories,
USA.
Kee, R.J., Rupley, F.M., Miller, J.A., 1996b. Chemkin II: A Fortran chemical kinetics
package for the analysis of gas-phase chemical kinetics, Report no. SAND89-
8009B. Sandia National Laboratories, USA.
Kurdyumov, V.N., Pizza, G., Frouzakis, C.E., Mantzaras, J., 2009. Dynamics of pre-
mixed flames in a narrow channel with a step-wise wall temperature. Combust.
Flame 156, 2190–2200.
Kyritsis, D.C., Coriton, B., Faure, F., Roychoudhury, S., Gomez, A., 2004. Optimization
of a catalytic combustor using electrosprayed liquid hydrocarbons for mesos-
cale power generation. Combust. Flame 139, 77–89.
Li, Y.H., Chen, G.B., Cheng, T.S., Yeh, Y.L., Chao, Y.C., 2013. Combustion characteristics
of a small-scale combustor with a percolated platinum emitter tube for ther-
mophotovoltaics. Energy 61, 150–157.
Mantzaras, J., 2008. Catalytic combustion of syngas. Combust. Sci. Technol. 180,
1137–1168.
Mantzaras, J., 2014. Catalytic Combustion of Hydrogen, Challenges, and Opportu-
nities. In: Dixon, A.G. (Ed.), Modeling and Simulation of Heterogeneous Cata-
lytic Processes, Advances in Chemical Engineering, Vol. 45. Elsevier Academic
Press Inc, San Diego, pp. 97–157.
Mantzaras, J., Appel, C., 2002. Effects of finite rate heterogeneous kinetics on
homogeneous ignition in catalytically stabilized channel-flow combustion.
Combust. Flame 130, 336–351.
Mantzaras, J., Appel, C., Benz, P., 2000. Catalytic combustion of methane/air mix-
tures over platinum: homogeneous ignition distances in channel flow config-
urations. Proc. Combust. Inst. 28, 1349–1357.
Mantzaras, J., Benz, P., 1999. An asymptotic and numerical investigation of homo-
geneous ignition in catalytically stabilized channel flow combustion. Combust.
Flame 119, 455–472.
Mantzaras, J., Bombach, R., Schaeren, R., 2009. Hetero-/homogeneous combustion
of hydrogen/air mixtures over platinum at pressures up to 10 bar. Proc. Com-
bust. Inst. 32, 1937–1945.
Michelon, N., Mantzaras, J., Canu, P., 2015. Transient simulation of the combustion
of fuel lean hydrogen/air mixtures in platinum coated channels. Combust.
Theor. Model. 19, 514–548.
Norton, D.G., Wetzel, E.D., Vlachos, D.G., 2004. Fabrication of single-channel cata-
lytic microburners: effect of confinement on the oxidation of hydrogen/air
mixtures. Ind. Eng. Chem. Res. 43, 4833–4840.
OpenFOAM, 2014. ⟨www.openfoam.org⟩, The open source CFD toolbox.
Pizza, G., Frouzakis, C.E., Mantzaras, J., Tomboulides, A.G., Boulouchos, K., 2010a.
Three-dimensional simulations of premixed hydrogen/air flames in microtubes.
J. Fluid Mech. 658, 463–491.
Pizza, G., Mantzaras, J., Frouzakis, C.E., 2010b. Flame dynamics in catalytic and non-
catalytic mesoscale microreactors. Catal. Today 155, 123–130.
Pizza, G., Mantzaras, J., Frouzakis, C.E., Tomboulides, A.G., Boulouchos, K., 2009.
Suppression of combustion instabilities of premixed hydrogen/air flames in
microchannels using heterogeneous reactions. Proc. Combust. Inst. 32,
3051–3058.
Raja, L.L., Kee, R.J., Deutschmann, O., Warnatz, J., Schmidt, L.D., 2000. A critical
evaluation of Navier-Stokes, boundary-layer, and plug-flow models of the flow
and chemistry in a catalytic-combustion monolith. Catal. Today 59, 47–60.
Reinke, M., Mantzaras, J., Schaeren, R., Bombach, R., Kreutner, W., Inauen, A., 2002.
Homogeneous ignition in high-pressure combustion of methane/air over pla-
tinum: comparison of measurements and detailed numerical predictions. Proc.
Combust. Inst. 29, 1021–1029.
Schneider, A., Mantzaras, J., Bombach, R., Schenker, S., Tylli, N., Jansohn, P., 2007.
Laser induced fluorescence of formaldehyde and Raman measurements of
major species during partial catalytic oxidation of methane with large H_2O and
CO_2 dilution at pressures up to 10 bar. Proc. Combust. Inst. 31, 1973–1981.

Schultze, M., Mantzaras, J., 2013. Hetero-/homogeneous combustion of hydrogen/air mixtures over platinum: Fuel-lean versus fuel-rich combustion modes. Int. J. Hydrogen Energy 38, 10654–10670.

Schultze, M., Mantzaras, J., Bombach, R., Boulouchos, K., 2013. An experimental and numerical investigation of the hetero-/homogeneous combustion of fuel-rich hydrogen/air mixtures over platinum. Proc. Combust. Inst. 34, 2269–2277.

Seshadri, V., Kaisare, N.S., 2010. Simulation of hydrogen and hydrogen-assisted propane ignition in Pt catalyzed microchannel. Combust. Flame 157, 2051–2062.

Seyed-Reihani, S.A., Jackson, G.S., 2004. Effectiveness in catalytic washcoats with multi-step mechanisms for catalytic combustion of hydrogen. Chem. Eng. Sci. 59, 5937–5948.

Stefanidis, G.D., Vlachos, D.G., 2009. High vs. low temperature reforming for hydrogen production via microtechnology. Chem. Eng. Sci. 64, 4856–4865.

Stefanidis, G.D., Vlachos, D.G., Kaisare, N.S., Maestri, M., 2009. Methane steam reforming at microscales: operation strategies for variable power output at millisecond contact times. AIChE J. 55, 180–191.

Tan, Y.W., Croiset, E., Douglas, M.A., Thambimuthu, K.V., 2006. Combustion characteristics of coal in a mixture of oxygen and recycled flue gas. Fuel 85, 507–512.

Um, D.H., Kim, T.Y., Kwon, O.C., 2014. Power and hydrogen production from ammonia in a micro-thermophotovoltaic device integrated with a micro-reformer. Energy 73, 531–542.

Woodside, W., Messmer, J.H., 1961. Thermal conductivity of porous media. I. unconsolidated sands. J. Appl. Phys. 32, 1688–1699.

Yang, W.M., Jiang, D.Y., Chou, S.K., Chua, K.J., Karthikeyan, K., An, H., 2012. Experimental study on micro modular combustor for micro-thermophotovoltaic system application. Int. J. Hydrogen Energy 37, 9576–9583.

Yoshida, K., Tanaka, S., Tomonari, S., Satoh, D., Esashi, M., 2006. High-energy density miniature thermoelectric generator using catalytic combustion. J. Microelectromech. Syst. 15, 195–203.

Zheng, X., Mantzaras, J., 2014. An analytical and numerical investigation of hetero-/homogeneous combustion with deficient reactants having larger than unity Lewis numbers. Combust. Flame 161, 1911–1922.